

1 **Revision 1**

2 **Cation partitioning among crystallographic sites based on bond-length constraints in**
3 **tourmaline-supergroup minerals**

4
5 Bačík P., Fridrichová J.

6
7 Comenius University in Bratislava, Faculty of Natural Sciences, Department of Mineralogy
8 and Petrology, Mlynská dolina, 842 15 Bratislava, Slovak Republic; peter.bacik@uniba.sk

9
10 **Running title: Cation partitioning in tourmaline-supergroup minerals**

11
12 **ABSTRACT**

13 Theoretical bond-length calculations from ideal bond valences for each ion and
14 coordination allows for the prediction of ion site preference and partitioning in tourmaline
15 structures at low-pressure conditions. A comparison of calculated data with published bond-
16 length values enables the determination of the range of structurally stable bond lengths with a
17 minimal induced distortion – the “Goldilocks zone”. The calculations provided following
18 conclusions: the *B*-site occupancy is strictly limited to B^{3+} ; the *T* site can freely accommodate
19 not only Si^{4+} , but also B^{3+} and Al^{3+} , although these substituents require shrinkage and
20 expansion of the TO_4 tetrahedron, respectively, and the Be^{2+} substitution results in a
21 significant difference in charge. Satisfactory bond lengths for octahedral sites were calculated
22 for Al^{3+} (*Z*-site preference), Ti^{4+} , Mn^{3+} , Ga^{3+} , V^{3+} , Fe^{3+} (mixed preference), Mg^{2+} , Fe^{2+} , Li^+ ,
23 Mn^{2+} , Ni^{2+} , Zn^{2+} , Cu^{2+} , Sc^{3+} and Zr^{4+} (*Y*-site preference). Another group of cations, which
24 includes U^{4+} , Th^{4+} , Y^{3+} and lanthanoids from Tb to Lu and Ce^{4+} , have significantly longer
25 bonds than typical *Y*-O and very short bonds for the *X* site; therefore, it is likely they would
26 prefer an octahedron. The empirical bond length for the *X* site is met with Na^+ , Ca^{2+} , Sr^{2+} ,
27 Pb^{2+} and lanthanoids from La to Gd, while K, Rb and Cs are too large in the low-pressure
28 conditions. However, the final tourmaline composition results from interaction of the structure
29 with the genetic environment in terms of P-T-X and geochemical conditions. This results in
30 structural and environmental constraints that limit the incorporation of elements into the

31 structure. Consequently, major elements, such as Si, Al, B, Mg, Fe, Na and Ca usually occur
32 in abundance, whereas other elements (V, Cr, Mn, Ti, Pb) could form end-member
33 compositions, but rarely do because of their low abundance in the environment. The elements
34 with contents limited to trace amounts have either structural (Be, C, REE, Rb, Cs, U, Th) or
35 geochemical (Zr^{4+} , Sc^{3+} and Sr^{2+}) limits. However, environmental properties, such as high
36 pressure or specific local structural arrangements can overcome structural constraints and
37 enable the incorporation of elements (K).

38

39 ***Key words:*** tourmaline supergroup; crystal chemistry; bond length calculation; cation
40 occupancy; trace elements

41

42

43 Introduction

44 Tourmaline supergroup minerals are cyclosilicates having the generalized
45 structural formula $XY_3Z_6(T_6O_{18})(BO_3)_3V_3W$, where the most common ions (or vacancy) at
46 each site are the following: $X = Na^+, K^+, Ca^{2+}$, and vacancy; $Y = Li^+, Fe^{2+}, Mg^{2+}, Mn^{2+}, Al^{3+},$
47 Fe^{3+} , and Cr^{3+} ; $Z = Mg^{2+}, Al^{3+}, Fe^{3+}$, and Cr^{3+} ; $T = Si^{4+}, Al^{3+}$, and B^{3+} ; $B = B^{3+}$; $V = (OH)^-$ and
48 O^{2-} ; and $W = (OH)^-, F^-$, and O^{2-} (Henry et al. 2011). Their particular structure contains 5
49 different cationic crystallographic sites with various coordinations – one tetrahedral T site,
50 two octahedral Z and Y sites, a polyhedral 9-coordinated X site, a triangular B site, and 8
51 different anionic sites – O1-O8 (Donnay and Buerger 1950). The structural complexity thus
52 results in large variability of chemical elements, which can be incorporated in the tourmaline
53 structure. The major elements include Si and B with small ionic radii, slightly larger Al, Mg,
54 Fe, Li, Mn, Cr, V, and Ti, and also the largest Na, Ca and K. Anionic sites comprise dominant
55 amount of O (as O^{2-} and OH^-) and usually a subordinate amount of F (Henry et al. 2011) or
56 Cl (Bačík et al. 2015b).

57 Many other elements can occupy a tourmaline structure in minor to trace amounts. These
58 include nearly the entire periodic table. Trace elements in tourmaline measured at the
59 micrometer scale become important tracers of the rock evolution and fluids interacting with
60 tourmaline. Tourmalines from various host environments can show a distinct chemical
61 signature of their host, such as increased Li concentrations in evolved magmatic rocks (e.g.,
62 Keller et al. 1999; Selway et al. 1999, 2000), anomalous Sn concentrations in Sn deposits
63 (Jiang et al. 1999; Williamson et al. 2000) and enrichment in Ni, V and Cr in metabasic rocks
64 and metabauxites (Henry and Dutrow 2001; Marschall et al. 2004). Subduction-zone fluids
65 and their impact on arc-magmatism signatures were modelled based on ratios of Ba, Th, La
66 and Sm (Van Hinsberg et al. 2017). Trace amounts of Sr, Sc, V, Ni, Pb, Zr, Ta, Nb, Cr, Ga
67 and Sn and REE have been used as proxies for mineralizing fluids in ore deposits and in other
68 rock environments (Duchoslav et al. 2017; Hazarika et al. 2017; Hong et al. 2017; Kalliomäki
69 et al. 2017). Relatively high Cl contents in tourmaline are used to establish the unusual
70 hydrothermal setting for altered dioritic porphyries associated with a gold deposit (Bačík et al.
71 2015b).

72 However, due to their low content, it is usually not possible to determine the position of
73 these minor and trace elements exactly in the tourmaline structure based only on the chemical
74 and structural data. Although the site occupancy usually follows Goldschmidt rules, structural
75 and bond-valence requirements may result in disorder with various interchanging cations

76 (Grice and Ercit 1993; Hawthorne et al. 1993). Moreover, the tourmaline structure can
77 accommodate ions which usually do not have an appropriate ionic radius for any structural
78 site in tourmaline (Bačík et al. 2015b). However, some assignments can be made based on
79 bond-length constraints for each ion at each site. Bond lengths can be derived from structural
80 data but can be applied only on ions which are abundant in the structure. However, theoretical
81 bond-length calculation from ideal bond valences for each ion and coordination can indicate
82 ion site preference in the structure. This could also help in the identification of internal
83 crystal-chemical and external genetic factors (including geochemical and P-T-X conditions)
84 that influence element partitioning, as well as the final tourmaline composition.

85

86 **Topology of tourmaline crystal structure**

87 Tourmaline-group minerals have a relatively complex structure. The main structural
88 element is built from a 3D framework of edge-connected ZO_6 octahedra, interconnected by
89 periodically distributed structural “islands” (Fig. 1). These comprise six-member rings of TO_4
90 tetrahedra, triplets of YO_6 octahedra, 9-coordinated X sites, and BO_3 triangles (Bosi 2018).
91 Chains of ZO_6 octahedra are oriented in the c direction and provide support for the structure,
92 but also have sufficient flexibility for any local or long-distance structural distortion (Fig. 2).
93 Moreover, their orientation in the c direction manifests in the usual long-prismatic tourmaline
94 crystal habit (Bačík et al. 2015a).

95 ***TO₄ tetrahedron***

96 The most apparent feature of the tourmaline structure is represented by a ring of six TO_4
97 tetrahedra, which are connected by the pairs of O^{2-} anions (Fig. 3). The apical atoms O (O6)
98 are directed towards the same ($-c$) pole of crystal, which is the basis for the crystallographic
99 asymmetry (Donnay and Buerger 1950; Barton Jr. 1969). Each TO_4 tetrahedron shares O
100 anions with the T ($2\times$), Y , Z ($3\times$) and X ($2\times$) sites (Fig. 3). They have the lowest distortion in
101 bond lengths (Δ – the formulae for each site are in Ertl et al. 2002) from all cation sites, which
102 have Δ in the following general order: $T < Z < Y < X$ (Ertl et al. 2002). This is likely given by
103 their small size, high charge, and rigidity compared to other polyhedra (Ertl et al. 2002).
104 However, a correlation between the size of cations occupying the X site and the bond-angle
105 distortion of tetrahedra was found (Foit and Rosenberg 1979; Ertl et al. 2002). The T -site
106 bond-angle distortion increased from 4.73 to 16.07 in accordance with the X-site charge,
107 which results from sharing six of the nine ligands with XO_9 polyhedron (Ertl et al. 2002). The

108 divalent X -site cations (Ca and other divalent cations) shift O4 and O5 bonds inwards to
109 accommodate at the X site with smaller ionic radii.

110 ***Triangular BO_3 groups***

111 Triangular BO_3 groups lie parallel to the plane (0001) and connect to the vertices of ZO_6
112 and YO_6 octahedra (Fig. 4). The BO_3 group shares O with Z ($4\times$), Y ($2\times$), and X ($3\times$) sites. The
113 presence of vacancies at B site was assumed to be possible, but with no spectroscopic or
114 structural evidence (Grice and Ercit 1993; Hawthorne 1996). A substitution mechanism that
115 requires vacancies at B would produce unacceptably short H- Y and H- Z bond lengths in all
116 cases except one, where H atoms at $x = 0.94$, $y = 0.06$, $z = 0.72$ can be bonded to O(2), only if
117 the X site is vacant (Hawthorne 1996). Therefore, the presence of B -site vacancies is highly
118 unlikely for these reasons.

119 ***ZO_6 and YO_6 octahedra***

120 The rings of tetrahedra are connected to two types of octahedra – ZO_6 and YO_6 . The ZO_6
121 octahedron (Fig. 5) is smaller than the YO_6 octahedron and is less distorted in terms of bond-
122 length distortion (Ertl et al. 2002), as well as in terms of angular distortion and quadratic
123 elongation (Bosi and Lucchesi 2007). It is connected to the T ($2\times$), Z ($3\times$), Y and B ($2\times$) sites.

124 Foit and Rosenberg (1979) showed on a number of tourmaline samples that an angular
125 distortion of the ZO_6 octahedron negatively correlates to $\langle Y-O \rangle$ bond length. However, data
126 indicated a high negative correlation between the bond-angle distortion of the ZO_6 octahedron
127 and $\langle Y-O \rangle$ in all tourmalines, in which O3 (V) site is occupied by 3 (OH) pfu (Ertl et al.
128 2002). The only exception was in buergerite, in which O is dominant at the V site (OH = 0.29
129 apfu, Dyar et al. 1998). Since the V site represents a vertex of ZO_6 octahedron, it can be
130 presumed that the occupation of this site affects the degree of Δ in octahedron, which is
131 unconstrained (Ertl et al. 2002).

132 The YO_6 octahedron is more regular with a larger size than Z (Henry and Dutrow 1996).
133 The YO_6 octahedron is connected by O atoms with X ($2\times$), T ($2\times$), Z ($2\times$), and B ($2\times$) sites
134 (Fig. 6). Changes in bond and angular distortions of the YO_6 octahedron are larger than that of
135 the ZO_6 octahedron and are influenced by both the size of the central cation, as well as the
136 actions of neighbouring polyhedra. Quite commonly, it is difficult to separate the effects of
137 individual factors (Ertl et al. 2002). An influence of the central cation on the Δ of the
138 octahedron decreases from Li-Al tourmalines with the largest distortion to Mg tourmalines
139 (dravite, uvite) with the least distortion. Therefore, the smallest cations (Ti, Al) cause the

140 greatest distortion (Ertl et al. 2002). Similarly, a significant difference in the size of the
141 cations in the X and Y sites induces local disorder and distortion in the YO_6 octahedron
142 (MacDonald and Hawthorne 1995).

143 ***XO₉ polyhedron***

144 The X site with the coordination number 9 is trigonal antiprism, which is located along a
145 threefold symmetry axis. The XO_9 polyhedron is connected through O atoms to T ($6\times$), Y ($3\times$),
146 and B ($3\times$) sites (Fig. 7).

147 The reasons for distortion in bond lengths of XO_9 polyhedron are not certain, but it is
148 possible to infer the influence of the X , Y and W site occupancy. Tourmalines with high
149 contents of Li and Al (>1 Li apfu) and a relatively high content of F have higher Δ of XO_9
150 polyhedron – the highest Δ was found in fluor-liddicoatite (Ertl et al. 2002). The size of the
151 cation occupying the XO_9 polyhedron is positively correlated with the $X-O_2$ distance (Ertl et
152 al. 2001), which may also affect the distortion in the XO_9 polyhedron (Ertl et al. 2002). Na-
153 bearing, Li-, and F-poor tourmalines generally have smaller Δ (olenite 1.04, schorl 1.33) than
154 Ca-dominant tourmalines (fluor-liddicoatite 4.47, uvite 3.06) (Ertl et al. 2002)

155

156 **Methods**

157 Bond-length calculations are based on the following equation:

$$158 \quad d_{ij} = R_0 - b \ln v_{ij}$$

159 where d_{ij} is the bond length (in Å) between the two given ions, the bond valence (v_{ij})
160 measures bond strength (in vu – valence units), R_0 is the length of a single bond (for which v_{ij}
161 = $1 vu$), and b is the universal parameter for each bond (Brown 2006). The R_0 and b values for
162 each cation from the list of Gagné and Hawthorne (2015) were used, since this list provides
163 the most current and consistent data on the bonding parameters. For more details, see Bačík
164 and Fridrichová (2019). Bond lengths (Table 1) were calculated only for the most common
165 major, minor, and trace elements occurring in tourmaline, although a similar approach can be
166 used for any chemical element.

167 Empirical average bond lengths (Table 2) were calculated from structural-refinement data
168 of natural tourmaline samples collected in the American Mineralogist Crystal Structure
169 Database (Downs and Hall-Wallace 2003). Two methods were used for calculations with
170 regards to the available data: (1) calculation of average from samples with the composition

171 closest to the end member, if the composition was less than 0.3 apfu deviated from the full
172 site occupancy (${}^T\text{Si}$, ${}^B\text{B}$, ${}^Y\text{Mg}$, ${}^Y\text{Fe}$); (2) calculation of bond length, assuming full site
173 occupancy from the trend line calculated as a linear equation from the samples, with the
174 composition deviating more than 0.3 apfu of selected element from the full site occupancy
175 (${}^T\text{B}$, ${}^Y\text{Mn}$, ${}^Y\text{Li}$, ${}^X\text{Na}$, ${}^X\text{Ca}$, ${}^X\Box$), (3) use of the published data (${}^Z\text{Al}$ – Bosi and Andreozzi 2013).

176

177 **Results**

178 ***TO₄ tetrahedron***

179 The *T* site is dominantly occupied by Si^{4+} . The calculated Si^{4+} -O distance of 1.624 Å is
180 very similar to the empirical bond length of 1.621 Å (Table 1, Fig. 8). There are two typical
181 substituents for Si^{4+} – Al^{3+} and B^{3+} . Tetrahedral Al^{3+} have longer bonds (1.746 Å) and B^{3+}
182 shorter bonds (1.475 Å calculated, 1.482 Å empirical) than Si^{4+} . Consequently, B^{3+} shrinks
183 and Al^{3+} expands the tetrahedron. If any Be^{2+} was present in tourmaline structure, it would
184 prefer the *T* site with 1.635 Å calculated bond length. Other cations form very long bonds
185 (Ti^{4+} 1.819 Å, Fe^{3+} 1.870 Å); therefore, their presence at the *T* site is unlikely.

186 ***BO₃ site***

187 Boron is the only cation occupying the triangular B site. The calculated B^{3+} -O bond
188 length of 1.372 Å is similar to the empirical average bond length (Table 1). This indicates that
189 B-O bond in tourmaline is almost ideal, allowing only negligible variations. Other possible
190 cations have much larger calculated bond lengths (Si^{4+} 1.512 Å, Be^{2+} 1.594 Å) excluding their
191 possible substitution. In contrast, the bond length calculated for C^{4+} -O bond in triangular
192 coordination with 1.284 Å is significantly smaller than both the empirical data and calculated
193 B^{3+} -O bond length.

194 ***ZO₆ and YO₆ octahedron***

195 The octahedral *Z* site is usually dominated by Al^{3+} with the empirical distance of 1.906 Å
196 (Bosi and Andreozzi 2013) and calculated Al-O bond length of 1.904 Å (Fig. 9a). Shorter
197 empirical bond length results from angular and bond-length distortion of the ZO_6 octahedron.
198 Smaller bond lengths were calculated only for Si^{4+} (1.782 Å) and Be^{2+} (1.755 Å), which have
199 not yet been reported in octahedral coordination in tourmaline. All other cations have larger
200 octahedral bond lengths; Ti^{4+} , Mn^{3+} , Ga^{3+} and Cr^{3+} below 2.00 Å, V^{3+} and Fe^{3+} slightly larger

201 than 2.00 Å, Mg²⁺, Fe²⁺, Li⁺, Mn²⁺, Ni²⁺, Zn²⁺, Cu²⁺, Sc³⁺, Zr⁴⁺ and Bi⁵⁺ between 2.09 and
202 2.20 Å (Fig. 9).

203 The last group of cations which could occupy octahedral sites include cations with bond
204 lengths between 2.20 and 2.30 Å (Fig. 9b). These are usually only in trace amounts and
205 include U⁴⁺, Th⁴⁺, Y³⁺ and lanthanoids from Tb³⁺ to Lu³⁺ (HREE). Moreover, Ce⁴⁺ has a bond
206 length of 2.217 Å. These cations are not excluded, but their proportion is very limited and
207 would cause large distortion of the YO₆ octahedra, if present. Those with a bond length larger
208 than 2.30 Å (LREE from La³⁺ to Gd³⁺, Bi³⁺, Pb²⁺) are highly unlikely to occupy octahedra in
209 tourmaline.

210 ***XO₉ polyhedron***

211 Based on the empirical data, the bond lengths at the X site vary between 2.609 (Ca²⁺) and
212 2.692 (Na⁺) (Fig. 10). A perfect match with these bond lengths was calculated for Na⁺ (2.618
213 Å), Sr²⁺ (2.678 Å) and Pb²⁺ (2.697 Å). The calculated Ca-O bond length of 2.522 Å is
214 significantly shorter than empirical data and similar to Na-O.

215 Other monovalent cations, including K⁺, Rb⁺ and Cs⁺, have much larger bond lengths
216 (>2.90 Å) at low-P conditions, thus limiting their presence in the tourmaline structure almost
217 entirely. Barium also has a relatively large bond length (2.834 Å). In contrast, U⁴⁺, Th⁴⁺, Y³⁺,
218 lanthanoids from Tb³⁺ to Lu³⁺ (HREE) and Ce⁴⁺ have significantly smaller bond lengths
219 (<2.45 Å), which are probably too small for the X site. Only trivalent lanthanoids from La³⁺ to
220 Gd³⁺ with bond lengths similar to Ca⁺ could likely occupy the X site.

221

222 **Discussion**

223 ***The “Goldilocks zone” structural constraints***

224 For the understanding of crystal-chemical properties and the prediction of the site
225 occupancy in any mineral, the Goldschmidt rules determining the possibility of substitutions
226 based on ionic radii are most often used. However, the bond-length calculation also provides
227 several advantages. For example, it can be used for various coordinations and cation charges
228 quite flexibly, only requiring a proper calculation of the bond valence. Moreover, it can be
229 easily compared to empirical analytical data from a structural refinement, as evidenced here.

230 For the evaluation of the allowed site occupancy, the “Goldilocks zone” for each site can
231 be defined. This term is derived from the “Goldilocks principle”, indicating a narrow range of

232 proper conditions (“just the right amount”) for certain phenomena and is used in a wide range
233 of disciplines, including biology and medicine (Martin 2011; Shander and Ferraris 2017),
234 astronomy (Levenson 2011), mathematics (Bharali and Zimmer 2017), and even geology
235 (Miller et al. 2002; Junod and Jacquet 2019). Used here, it defines the zone of structurally
236 stable bond lengths with a minimal induced distortion. It can be defined empirically by the
237 largest and shortest possible bond lengths in the extreme near-to-end-member compositions,
238 or theoretically, based on the selected deviation value – we used 10% deviation from the
239 empirical bond lengths for the most common occupants of selected sites.

240 The “Goldilocks zone” of bond lengths for each site is influenced by the short-range
241 effects in local structural arrangements around specific sites. According to the Bond Valence
242 Model, there is a tendency for the sum of the bond valences (BVS) around each atom to
243 approach its formal valence (FV); if a significant mismatch between BVS and FV occurs, it is
244 indicative of strained bonds that lead to an instability of the structure (Brown 2006; Bosi
245 2018). Based on the valence-sum rule, Hawthorne (1996, 2002) and Bosi (2010, 2011, 2013)
246 evaluated possible atomic arrangements around O1 and O3. The local arrangements
247 conforming the closest to the valence-sum rule are those that are most likely to occur in the
248 structure (Hawthorne 2016). In turn, the influence of O at the O1 site has a strong impact on
249 the disorder in the Y and Z sites (Hawthorne 1996, 2002).

250 The structural strain resulting from the bond-valence requirements of ions with variable
251 FV can be relaxed by the distortion of structural polyhedra. Variations in the tourmaline
252 octahedral occupancy influence the geometry of both *Y* and *Z* octahedra. The irregularity at
253 these sites is larger, when the difference of the occupying cations charge is larger. Elbaite,
254 which has the largest charge difference between Li and Al, displays the largest irregularity of
255 both octahedra. In contrast, fluor-buergerite with trivalent Fe and Al have only small
256 irregularity of octahedral sites that closely approach ideal octahedral metrics in both cases.
257 These variations mainly occur at the shared edge of the ZO_6 and YO_6 octahedra – not only at
258 the O3, but also at O6 site (Bačík 2018). Moreover, the *Z*- and *Y*-site occupancy influences the
259 distortion at the neighboring sites. Extremely large ZO_6 octahedra in povondraite, occupied
260 mostly by Fe^{3+} and Mg^{2+} , expands the structure and allows for presence of large K^+ at the *X*
261 site (Grice et al. 1993; Žáček et al. 2000).

262 The structural stability requirements, however, also involve long-range structural effects.
263 They are mainly determined by spatial/steric constraints (imposed by translational symmetry)
264 that restrict the number of ways in which ions can be bonded to each other in a three-

265 dimensional space. In tourmaline, the three-dimensional framework of the ZO_6 polyhedra
266 must be able to accommodate the structural islands (Bosi 2018). On the basis of 127 structure
267 refinement (SREF) data, which were later extended to 322 datasets (Bosi 2018), a structural
268 stability field was determined for tourmaline as a function of $\langle Y-O \rangle$ and $\langle Z-O \rangle$, suggesting
269 that only limited variations between the $\langle Y-O \rangle$ and $\langle Z-O \rangle$ dimensions can be tolerated by the
270 structure (Bosi and Lucchesi 2007). Additionally, the influence of other structural motifs,
271 including tetrahedral rings and distribution of cations (Al^{3+} with the largest influence) among
272 structural sites (Bosi et al. 2010), also defines possible constraints for the determination of the
273 „Goldilocks zone“.

274

275 ***Determination of the “Goldilocks zone” for crystallographic sites***

276 For the determination of the “Goldilocks zone”, the relations between ideal and real
277 crystal structures must be considered. We can make some approximations using an
278 octahedron as an example of the coordination polyhedron.

279 As an initial approximation, we can consider an ideal octahedron (Fig. 11a). The largest
280 sphere, which is coordinated by six spheres, has the same radius as the largest circle
281 coordinated by 4-unit circles in the cross-section perpendicular to one of octahedron axis (Fig.
282 11b). The distance of circle centres corresponds to the bond length between the central cation
283 (R) and ligand (O) in octahedral coordination. It is equal to the square root of two squares of a
284 ligand ionic radius (Fig. 11b, outer circle). With regards to the O^{2-} ionic radius (1.36 Å in 3-
285 fold coordination, Shannon 1976), the R-O bond length is equal to 1.92 Å. By the subtraction
286 of O^{2-} ionic radius, we get the central-cation ionic radius of 0.56 Å (Fig. 11c). The ionic
287 radius of Al^{3+} in octahedral coordination is equal to 0.535 Å (Shannon 1976). It is very close
288 to the ideal value; consequently, isolated Al^{3+} -bearing octahedron should not be subjected to
289 any bond-length distortion in the rigid-sphere model. If any distortion occurs, it should be
290 attributed to the influence of surrounding polyhedra in a complex crystal structure.

291 As a second approximation, we need to involve the internal structure of the atomic shell
292 and electrostatic properties of bonds. The ideal Al-O bond length for octahedral coordination,
293 which is calculated using the bond-valence approach (Brown 2006), is slightly shorter – 1.904
294 Å. This indicates that an attractive electrostatic force of Al^{3+} results in significant shortening
295 of Al-O bonds compared to the ideal-octahedron model with bond-length determined by
296 cation+anion ionic radii. Individual Al-O bond lengths in the ZO_6 octahedron closely

297 approach 1.87 Å with an increasing Al content in tourmaline. For Al and other *s* and *p*
298 elements, including Li, B, Si, Mg, Na, and Ca as the most common in tourmaline, we can
299 assume homogeneous elongation or shortening of bonds in this approximation.

300 The situation gets more complicated for *d* elements, whose internal structure with unfilled
301 *d* orbitals allows for the reduction of symmetry due to Jahn-Teller distortion (Jahn et al.
302 1937). This was observed for Fe²⁺, Mn³⁺, and Cu²⁺ in similar silicates, such as epidote,
303 gadolinite-hingganite, chlorite and mica, as well as in tourmaline (Burns and Strens 1967;
304 Faye 1968; Ito and Hafner 1974; Burns and Hawthorne 1996; Bačík et al. 2014, 2017; Ertl et
305 al. 2015; Fridrichová et al. 2018). However, this distortion can be described in the second
306 approximation.

307 The third approximation involves the external short-range and long-range effects of
308 neighbouring atoms. Once again, Al at the tourmaline *Z* site can be used as an example. Both
309 the *Z*-O7 and *Z*-O8 bonds have a length close to 1.87 Å in the Al dominant compositions.
310 However, both the *Z*-O3 and *Z*-O7' bonds are longer. The *Z*-O3 bond length is expanded due
311 to OH group dominance at the O3 site, which also causes the elongation of the *Z*-O7' bond
312 (Bačík 2018). The O-H bond valence, which is slightly lower than 1 *vu* due to the hydrogen
313 bond, reduces in the *Z*-O3 bond valence to 0.36 *vu* (Bačík 2018). However, the *Z*-O6 bond
314 length in the most Al-rich tourmalines is distinctly lower, since it balances the bond valences
315 in a complex relationship between YO₆ and ZO₆ octahedra (Bačík 2018).

316 Consequently, the prediction of bond lengths in real structures, which is based on simple
317 idealistic bond-valence calculations, has its limits. However, it can be a good approximation
318 for the prediction of site occupancies.

319

320 ***Partitioning of cations***

321 The “Goldilocks zone” is quite narrow for small sites, such as *B* and *T* in tourmaline, but
322 larger in sites with a higher coordination number. It is well-documented on the tetrahedral *T*
323 site, which allows for only partly limited substitution of Al³⁺ and B³⁺, as well as on the *B*-site
324 occupancy, which is strictly limited to B³⁺. The substitution of B³⁺ for Si⁴⁺ at the *T* site is
325 more common in HP/UHP conditions, which compress the structure to enable this substitution
326 (Hughes et al. 2000; Ertl et al. 2006; Kutzschbach et al. 2016). Other structural short-range
327 effects can also allow for the substitution of B³⁺ for Si⁴⁺; e.g. in tourmalines of fluor-

328 liddicoatite-elbaite series – the excess of Al at the *Y* site in $^Y(\text{Al}_2\text{Li})$ compositions results in
329 the presence of tetrahedral B (Ertl et al. 2006, 2018).

330 In contrast, extensive “tschermak-type” $\text{Al}_2\text{Si}_{-1}\text{Mg}_{-1}$ substitution indicates high-grade
331 metamorphism in the Al-rich and, to a lesser extent, silica-poor environment (Henry and
332 Dutrow 1996; Ertl et al. 2018). Higher ^TAl is quite often connected with oxy-tourmalines
333 (Cempírek et al. 2006; Bosi et al. 2010, 2017; Bačík et al. 2013, 2015b). In short, relatively
334 high amounts of ^TAl may be expected in Mg- and/or Fe^{2+} -rich tourmalines in aluminous bulk
335 compositions and high-temperature metamorphic conditions. Significant amounts of ^TAl are
336 also found in pegmatitic Al-rich and Li-bearing tourmaline species including Li-rich schorl,
337 elbaite, fluor-liddicoatite, olenite, “oxy-rossmanite” (Cámara et al. 2002; Bosi et al. 2005;
338 Lussier et al. 2008; Ertl et al. 2018). Moreover, adachiite, which was found in a hydrothermal
339 vein (with margarite and diaspore) crosscutting a lateritic metamorphic rock in Japan, is the
340 first end-member of the tourmaline supergroup formed via Tschermak-like substitution
341 (Nishio-Hamane et al. 2014).

342 Octahedral sites have the largest variety of possibilities of occupying cations. Bond-
343 length calculations can also help determine site preference for each cation. The *Z* site prefers
344 smaller cations that are more similar to Al^{3+} – Ti^{4+} , Mn^{3+} , Ga^{3+} , and Cr^{3+} with bond lengths
345 below 2.00 Å. Cations with bond lengths slightly larger than 2.00 Å – V^{3+} and Fe^{3+} may have
346 no significant site preference at low concentrations. Cations with bond lengths between 2.09
347 and 2.20 Å – Mg^{2+} , Fe^{2+} , Li^+ , Mn^{2+} , Ni^{2+} , Zn^{2+} , Cu^{2+} , Sc^{3+} and Zr^{4+} – prefer a larger YO_6
348 octahedron. If we consider that the average *Z*–O bond length in povondraite with 4.29 apfu
349 Fe^{3+} , 1.36 apfu Mg^{2+} and 0.32 apfu Al^{3+} was 2.007 Å (Grice et al. 1993), this value can be
350 used for discrimination of cation site-occupancy preference. Those forming bonds shorter
351 than 2.01 apfu tend to prefer the *Z* site, while larger cations usually occupy the *Y* site.
352 However, this cannot be considered a fixed rule when other structural features occur as
353 discussed later.

354 This is in accordance with the preference sequences of $^Y\text{Fe}^{3+} > ^Y\text{V}^{3+} > ^Y\text{Cr}^{3+} > ^Y\text{Al}^{3+}$ and
355 $^Z\text{Al}^{3+} > ^Z\text{Cr}^{3+} > ^Z\text{V}^{3+} > ^Z\text{Fe}^{3+}$ for trivalent and $^Y\text{Mn}^{2+} > ^Y\text{Fe}^{2+} > ^Y\text{Co}^{2+} > ^Y\text{Mg}^{2+} > ^Y\text{Ni}^{2+}$ and
356 $^Z\text{Ni}^{2+} > ^Z\text{Mg}^{2+} > ^Z\text{Co}^{2+} > ^Z\text{Fe}^{2+} > ^Z\text{Mn}^{2+}$ for divalent cations based on the ionic radii (Bosi
357 2018). Select relative element partitioning among tourmaline and other coexisting minerals in
358 (mostly) metapelitic rocks was determined as follows: B: tourmaline >> muscovite >
359 sillimanite > biotite, plagioclase > staurolite, garnet; Mg: tourmaline >> staurolite > gahnite;
360 Na: tourmaline > plagioclase; Ca: plagioclase > tourmaline; Li: staurolite > chlorite >

361 cordierite > biotite > muscovite > tourmaline, garnet, chloritoid; F: tourmaline > biotite >
362 muscovite; Cr: chromite > tourmaline > margarite > muscovite > corundum; Ni: talc >
363 tourmaline > staurolite > muscovite > gahnite; Co: tourmaline > staurolite > muscovite >
364 gahnite; Zn: gahnite > staurolite > tourmaline > muscovite; LREE: average continental crust >
365 tourmaline (Henry and Dutrow 1996, 2001, 2018).

366 The excellent correlation between the $\langle X-O \rangle$ distance and the average ionic radius of the
367 X -site occupants shows that the $\langle X-O \rangle$ distance is essentially dependent on the X -site
368 occupants (Ertl and Tillmanns 2012). Consequently, calculated $X-O$ bond lengths allow for
369 great prediction of the X -site occupants. Cations, which could occupy the X site, can be
370 divided into three groups. The first group comprises cations with calculated bond lengths
371 similar to the average empirical bond lengths – Na^+ , Ca^{2+} , Sr^{2+} and Pb^{2+} . These cations,
372 including Bi^{3+} (Ertl and Bačík 2020), have no bond-length constraints in occupying the X site.
373 The second group involves cations with significantly larger bond lengths in the order of Ba^{2+}
374 $< K^+ < Rb^+ < Cs^+$. The substitution of these cations is usually limited (limitation increases
375 progressively in the specified order) and their incorporation into the tourmaline structure in
376 significant amounts requires specific structural adjustments (Grice and Ercit 1993; Žáček et
377 al. 2000; Henry and Dutrow 2012; Berryman et al. 2015; Lussier et al. 2016) usually at
378 specific PT-conditions (Berryman et al. 2015; Lussier et al. 2016).

379 The last group of potential X -site occupants contains cations with significantly smaller
380 bond lengths and a higher charge compared to the typical X -site occupants, but a larger bond
381 length than octahedral cations. This group includes U^{4+} , Th^{4+} and REE^{3+} . The difference in
382 charge and bond lengths could be the clear structural limit for their amount in tourmaline –
383 there is no structural site in the tourmaline structure that matches their requirements perfectly.
384 As a consequence, their content is limited to trace amounts, even in a REE-rich environment,
385 such as in REE-rich NYF pegmatites (Bačík et al. 2012). However, on the basis of affinity to
386 selected crystallographic sites, it could be assumed that larger cations, including $LREE^{3+}$ –
387 La^{3+} to Gd^{3+} (but there is no clear border line) prefer the X site, while smaller $HREE^{3+}$ and
388 Ce^{4+} have an affinity to the Y site. However, LREE fit better into the X -site “Goldilocks zone”
389 than HREE at the Y site. This corresponds to the LREE preference observed in REE-bearing
390 tourmalines (Bačík et al. 2012 and references therein). Actinoids have no clear preference, but
391 U^{4+} with a smaller bond length would have stronger affinity to octahedral sites than Th^{4+} .

392

393 ***Crystal chemistry vs. genetic environment***

394 The partitioning of cations in tourmaline structural sites results from both internal
395 structural and external environmental factors. It is not easy to distinguish the roles played by
396 these factors, since they always act simultaneously. Nevertheless, because it is necessary to
397 attempt sorting out the roles played by internal and external factors, we have identified a few
398 possible ways of achieving this objective.

399 The specific case partitioning of minor and trace elements between tourmaline and melt
400 can be determined from partition coefficients of two phases. Major elements directly
401 influence the thermodynamic stability of the mineral and are thus controlled by a different
402 process from the one operating for the trace elements (Van Hinsberg 2011). Partition-
403 coefficients calculated by Van Hinsberg (2011) are invariably close to unity, which shows
404 that tourmaline is unable to significantly fractionate trace elements. Partitioning is systematic
405 and corresponds to predictions based on the lattice-strain theory, which allows element
406 valence and element site-occupancy to be determined from partitioning data. Results indicate
407 occupancy of Na, K, Rb, Ag, Sr, Ba and Pb at the *X* site, Mn, Co, Ni, Cu, Zn, Sc, V, Ga, Sb,
408 REE, Ti, Hf and Zr at the *Y* and *Z* sites, and Be at the *T* site (Van Hinsberg 2011). This
409 distribution corresponds well to our calculations.

410 Cation partitioning based on the bond-length constraints shows similarities to partition
411 coefficients. The “Goldilocks zone” is quite narrow at small sites, such as *B* and *T* in
412 tourmaline, but larger in sites with a higher coordination number. This is one of the limits for
413 site occupancy. Cations with a larger deviation from the “Goldilocks zone” can still be
414 accommodated at the respective sites, but their substitution is limited. This is the case of Al
415 and B at the *T* site – they substitute for Si, but only in a limited proportion. Similarly, the
416 proportion of REE in tourmaline is limited, although it can be abundant in the environment.
417 This is a result of deviation from both the *X*- and *Y*-site “Goldilocks zones”, as well as a
418 relatively high charge for the *X* site. However, on the basis of the data presented, if present,
419 REE likely divides between the *Y* (HREE) and *X* (LREE) site.

420 In contrast, some cations are perfectly placed in the “Goldilocks zone”, yet are usually
421 only in trace amounts or even below the detection limits of frequently used analytical
422 methods. This can be explained by external geochemical properties of the genetic
423 environment. Such elements can be fractionated into different minerals with better structural
424 properties for their accommodation. This is the case of Be²⁺ at the *T* site, which, due to its
425 small charge, prefers other minerals, most commonly beryl, chrysoberyl, etc. An increased Be

426 content was found in Al-rich tourmalines – 76 ppm Be in elbaite from the Himalaya Mine
427 pegmatite, California (Ertl et al. 2010c) and even 0.02 wt.% of BeO in olenite from Koralpe
428 metapegmatite, Austria (Kalt et al. 2001) with the formula refined to $T[\text{Si}_{4.89}\text{B}_{0.83}\text{Al}_{0.27}\text{Be}_{0.01}]$
429 (Ertl et al. 2007). The highest Be content is in tourmaline enriched in tetrahedral B^{3+} and can
430 also be well correlated with Al at the *Y* site with $r^2 = 0.969$ (Ertl et al. 2010c). This link to Al-
431 rich tourmalines suggests that Be^{2+} with a smaller charge than Si^{4+} , similarly to B^{3+} , can
432 effectively substitute at the tetrahedral site only in tourmalines with excess in charge at both
433 octahedral sites dominated by Al^{3+} . The increased Be content in tourmaline can be also linked
434 to generally low bulk Be content in pegmatite insufficient to form Be minerals such as
435 Koralpe metapegmatite, in which no Be minerals phases have been found (A. Ertl, personal
436 communication, October 29, 2020).

437 In fact, there are no significant examples of direct Be^{2+} for Si^{4+} substitutions. In the
438 majority of Be minerals, such as beryl (Auricchio et al. 1988), gadolinite-supergroup
439 minerals (Bačík et al. 2017), and sapphirine-supergroup minerals (Grew et al. 2008), Be^{2+}
440 occupies an independent tetrahedron that prefers substitution for Al^{3+} or B^{3+} instead of Si^{4+} . In
441 the sapphirine supergroup mineral khmaralite, Be distribution and the strong preference for
442 Be/Al mixing over Be/Si mixing appear to satisfy the bonding requirements for the bridging
443 of O atoms by minimizing the number of Be-O-Be and Be-O-Al linkages (Barbier et al.
444 1999). In other Be-bearing minerals in the sapphirine supergroup, Be^{2+} cations are found to
445 occupy some of the most polymerized *T* sites that share corners with three other *T* sites (Grew
446 et al. 2007). Consequently, the substitution of Be^{2+} in tourmaline limited may result from a
447 relatively low degree of TO_4 polymerization; only two corners are shared with other *T* sites.

448 Likewise, Bi^{5+} can form bonds inside the boundaries of the “Goldilocks zone” for the
449 octahedral sites; however, its higher charge limits possible substitutions allowing for its
450 presence in the tourmaline structure (Ertl and Bačík 2020).

451 Some other elements are commonly found only in trace amounts in the tourmaline
452 environment or are already bound to other minerals – Zr^{4+} , Sn^{4+} , Bi^{3+} , Sc^{3+} , Sr^{2+} . These
453 elements, if enriched, are usually well below 1 wt. % – Sn^{4+} up to 0.42 wt % SnO_2 (Yu and
454 Jiang 2003), Bi^{3+} up to 0.49 wt % Bi_2O_3 (Johnson et al. 1997). Although some of these are
455 usually present only in trace amounts in tourmaline, several can accumulate in specific
456 conditions – Ti^{4+} , Cr^{3+} , V^{3+} , Mn^{2+} , Cu^{2+} , Zn^{2+} , Ni^{2+} and Pb^{2+} . There were tourmaline crystals
457 enriched in Ti^{4+} (up to 4.62 wt % TiO_2 ; Vezzoni et al. 2018), Cu^{2+} (up to 3.51 wt % CuO ;

458 Vereshchagin et al. 2013; Ertl et al. 2015), Ni²⁺ (up to 3.96 wt % NiO; Baksheev and
459 Kudryavtseva 2004), and Zn²⁺ (up to 7.37 wt % ZnO; Pieczka et al. 2018).

460 Some of these common trace elements can accumulate in specific conditions to form end-
461 member composition. Divalent manganese is dominant in the *Y*-site cation in tsilaisite (Bosi et
462 al. 2012b), fluor-tsilaisite (Bosi et al. 2015) and celleriite (Bosi et al. 2020). Chromium forms
463 several mineral species – chromium-dravite (Rumyantseva 1983), oxy-chromium-dravite
464 (Bosi et al. 2012a), chromo-alumino-povondraite (Reznitskii et al. 2014) and vanadio-oxy-
465 chromium-dravite together with vanadium (Bosi et al. 2014a). Vanadium is dominant in
466 vanadio-oxy-dravite (Bosi et al. 2014b) and oxy-vanadium-dravite (Bosi et al. 2013). Pb-rich
467 fluor-liddicoatite and Pb-dominant analogue of fluor-liddicoatite were described in the
468 elbaite-subtype granitic Minh Tien pegmatite in northern Vietnam (Kubernátová and
469 Cempírek 2019). Recently, the first Ti-rich tourmaline end-member was described as
470 dutrowite (Biagioni et al. 2019).

471 The flexibility of the tourmaline structure may allow for the incorporation of elements
472 from outside the “Goldilocks zone”. The compression of the tourmaline structure under UHP
473 conditions allowed the incorporation of K into the structure of maruyamaite, which qualifies
474 for the end-member composition (Lussier et al. 2016). Recent experimental studies of K and
475 Na incorporation into dravitic tourmaline coexisting with a KCl-bearing fluid indicate that K
476 progressively increases at the *X*-site with an increase of pressure, temperature and KCl
477 concentration (Berryman et al. 2015). However, K can be introduced to the *X* site also in Fe³⁺-
478 rich tourmalines with a properly expanded structure at lower pressures (Grice and Ercit 1993;
479 Žáček et al. 2000; Henry and Dutrow 2012). Povondraite, which allows for the incorporation
480 of K into the *X* site, has a significantly expanded ZO₆ octahedron ($\langle Z-O \rangle = 2.007 \text{ \AA}$) and
481 consequently, *a* (16.186 Å), *c* (7.444 Å) and cell volume (1689 Å³) compared to ^ZAl-
482 dominant tourmalines usually with *a* < 16 Å, *c* < 7.3 Å and *V* < 1610 Å³ (Grice et al. 1993).
483 As a consequence, $\langle X-O \rangle$ increased to 2.738 Å in povondraite, while it is usually below 2.70
484 Å in ^ZAl-dominant tourmalines (Grice et al. 1993). It should also be mentioned that both
485 maruyamaite and povondraite are oxy-tourmalines. The distance between Na and H1 is 2.362
486 Å in oxy-dravite with occupancy of 0.245 H at the H1 site (Gatta et al. 2014). Interestingly
487 enough, the K content of 0.53 apfu is very similar to, yet slightly lower than the ^WO content of
488 0.60 apfu (Lussier et al. 2016). Therefore, the absence of H at the *W* site can minimize
489 electrostatic repulsion for a large cation at the *X* site, and it suggests that K prefers structural
490 arrangements of oxy-tourmalines.

491 Similar structural adjustment was observed in tourmaline crystallized in the Al-rich
492 environment in the Detva-Biely Vrch deposit, which resulted in the composition with a high
493 proportion of $V^{O^{2-}}$. This resulted in the shortening of $Y-V$ bond and subsequent incorporation
494 of the disproportionately large Cl^- anion at the W site (Bačík et al. 2015b).

495 However, there is a limitation for simple bond-length prediction of the site preference
496 because the short- and long-range structural constraints influence the cationic distribution.
497 This is manifested in various cation disorder reactions at octahedral sites. Along with the Al-
498 Mg disorder (Grice and Ercit 1993; Hawthorne et al. 1993), the Cr-Al and V-Al disorder
499 between Y and Z sites was documented (Bosi and Lucchesi 2004; Cempírek et al. 2013; Bosi
500 et al. 2017), as well as disordering of Fe over Y and Z sites with temperature in treated
501 samples (Bosi et al. 2019). These were explained by several factors: the Fe/(Fe+Mg) ratio
502 (Grice and Ercit 1993), influence of the W -site (Hawthorne 1996, 2002) and X -site occupancy
503 (Ertl et al. 2010a), structural deformations (Foit 1989; Bosi and Lucchesi 2007), pressure (Ertl
504 et al. 2010b), and temperature (Bosi 2011).

505

506 **Implications**

507 Understanding the factors that influence the partitioning of chemical elements, including
508 trace elements among crystallographic sites in structurally complex minerals, such as
509 tourmaline-super group minerals, is necessary for the proper determination of mineral
510 composition and decoding of genetic properties and processes during the crystallization.
511 Predictions from bond-valence constraints, which are based on a theoretical bond-length
512 calculation from ideal bond valences for each ion and coordination, are a useful tool for the
513 identification of the internal crystal-chemical factors that determine cation distribution.
514 Moreover, it allows for the determination of geochemical factors that influence tourmaline
515 composition when there is no structural constraint. Therefore, the implications of this type of
516 theoretical study are not limited only to structural and crystal-chemical issues, but also extend
517 to mineralogic-genetic, geochemical, petrological, or ore-deposit research. They also create
518 the basis for further study of cation distribution in the tourmaline structure, as well as
519 understanding of all structural factors and constraints.

520

521 **Acknowledgement:** We would like to express our gratitude to Ed Grew as the handling
522 editor, Darrell Henry, Ferdinando Bosi, Andreas Ertl and one anonymous reviewer for their

523 comments and suggestions greatly improving a quality of our paper. This work was supported
524 by the Slovak Research and Development Agency under the Contract no. APVV-18-0065.
525

526 **References**

- 527 Aurisicchio, C., Fioravanti, G., Grubessi, O., and Zanazzi, P.F. (1988) Reappraisal of the
528 crystal chemistry of beryl. *American Mineralogist*, 73, 826–837.
- 529 Bačík, P. (2018) The crystal-chemical autopsy of octahedral sites in Na-dominant
530 tourmalines: Octahedral metrics model unconstrained by the *Y,Z*-site disorder
531 assignment. *Journal of Geosciences (Czech Republic)*, 63, 137–154.
- 532 Bačík, P., and Fridrichová, J. (2019) The site occupancy assessment in beryl based on bond-
533 length constraints. *Minerals*, 9, 641.
- 534 Bačík, P., Uher, P., Ertl, A., Jonsson, E., Nysten, P., Kanický, V., and Vaculovič, T. (2012)
535 Zoned REE-enriched dravite from a granitic pegmatite in Forshammar, Bergslagen
536 Province, Sweden: An EMPA, XRD and LA-ICP-MS study. *Canadian Mineralogist*, 50,
537 825–841.
- 538 Bačík, P., Cempírek, J., Uher, P., Novák, M., Ozdín, D., Filip, J., Škoda, R., Breiter, K.,
539 Klementová, M., Ďuda, R., and others (2013) Oxy-schorl, $\text{Na}(\text{Fe}^{2+}_2\text{Al})\text{Al}_6\text{Si}_6\text{O}_{18}$
540 $(\text{BO}_3)_3(\text{OH})_3\text{O}$, a new mineral from Zlatá Idka, Slovak Republic and Příbyslavice, Czech
541 Republic. *American Mineralogist*, 98, 485–492.
- 542 Bačík, P., Fridrichová, J., Uher, P., Pršek, J., and Ondrejka, M. (2014) The crystal chemistry
543 of gadolinite-datolite group silicates. *Canadian Mineralogist*, 52, 625–642.
- 544 Bačík, P., Ertl, A., Števko, M., Giester, G., and Sečkář, P. (2015a) Acicular zoned tourmaline
545 (magnesio-foitite to foitite) from a quartz vein near Tisovec, Slovakia: The relationship
546 between crystal chemistry and acicular habit. *Canadian Mineralogist*, 53, 221–234.
- 547 Bačík, P., Koděra, P., Uher, P., Ozdín, D., and Jánošík, M. (2015b) Chlorine-enriched
548 tourmalines in hydrothermally altered diorite porphyry from the Biely vrch porphyry
549 gold deposit (Slovakia). *Canadian Mineralogist*, 53, 673–691.
- 550 Bačík, P., Miyawaki, R., Atencio, D., Cámara, F., and Fridrichová, J. (2017) Nomenclature of
551 the gadolinite supergroup. *European Journal of Mineralogy*, 29, 1067–1082.
- 552 Baksheev, I.A., and Kudryavtseva, O.E. (2004) Nickeloan tourmaline from the berezovskoe
553 gold deposit, Middle Urals, Russia. *Canadian Mineralogist*, 42, 1065–1078.
- 554 Barbier, J., Grew, E.S., Moore, P.B., and Su, S.C. (1999) Khmaralite, a new beryllium-
555 bearing mineral related to sapphirine: A superstructure resulting from partial ordering of

- 556 Be, Al, and Si on tetrahedral sites. *American Mineralogist*, 84, 1650–1660.
- 557 Barton Jr., R. (1969) Refinement of the crystal structure of buergerite and the absolute
558 orientation of tourmalines. *Acta Crystallographica Section B Structural Crystallography*
559 *and Crystal Chemistry*, 25, 1524–1533.
- 560 Berryman, E.J., Wunder, B., Wirth, R., Rhede, D., Schettler, G., Franz, G., and Heinrich, W.
561 (2015) An experimental study on K and Na incorporation in dravitic tourmaline and
562 insight into the origin of diamondiferous tourmaline from the Kokchetav Massif,
563 Kazakhstan. *Contributions to Mineralogy and Petrology*, 169, 28.
- 564 Biagioni, C., Bosi, F., Mauro, D., Skogby, H., Dini, A., and Zaccarini, F. (2019) Dutrowite,
565 IMA 2019-082. *CNMNC Newsletter* 53, *Eur. J. Mineral.*, 32.
- 566 Bosi, F. (2010) Octahedrally coordinated vacancies in tourmaline: a theoretical approach.
567 *Mineralogical Magazine*, 74, 1037–1044.
- 568 ——— (2011) Stereochemical constraints in tourmaline: From a short-range to a long-range
569 structure. *Canadian Mineralogist*, 49, 17–27.
- 570 ——— (2013) Bond-valence constraints around the O1 site of tourmaline. *Mineralogical*
571 *Magazine*, 77, 343–351.
- 572 ——— (2018) Tourmaline crystal chemistry. *American Mineralogist*, 103, 298–306.
- 573 Bosi, F., and Andreozzi, G.B. (2013) A critical comment on Ertl et al. (2012): “limitations of
574 Fe 2+ and Mn2+ site occupancy in tourmaline: Evidence from Fe2+- and Mn2+-rich
575 tourmaline.” *American Mineralogist*, 98, 2183–2192.
- 576 Bosi, F., and Lucchesi, S. (2004) Crystal chemistry of the schorl-dravite series. *European*
577 *Journal of Mineralogy*, 16, 335–344.
- 578 ——— (2007) Crystal chemical relationships in the tourmaline group: Structural constraints
579 on chemical variability. *American Mineralogist*, 92, 1054–1063.
- 580 Bosi, F., Andreozzi, G.B., Federico, M., Graziani, G., and Lucchesi, S. (2005) Crystal
581 chemistry of the elbaite-schorl series. *American Mineralogist*, 90, 1784–1792.
- 582 Bosi, F., Balić-Žunić, T., and Surour, A.A. (2010) Crystal structure analyses of four
583 tourmaline specimens from the Cleopatra’s Mines (Egypt) and Jabal Zalm (Saudi
584 Arabia), and the role of Al in the tourmaline group. *American Mineralogist*, 95, 510–
585 518.

- 586 Bosi, F., Reznitskii, L., and Skogby, H. (2012a) Oxy-chromium-dravite, $\text{NaCr}_3(\text{Cr}_4\text{Mg}_2)$
587 $(\text{Si}_6\text{O}_{18})(\text{BO}_3)_3(\text{OH})_3\text{O}$, a new mineral species of the tourmaline supergroup. American
588 Mineralogist, 97, 2024–2030.
- 589 Bosi, F., Skogby, H., Agrosi, G., and Scandale, E. (2012b) Tsilaisite,
590 $\text{NaMn}_3\text{Al}_6(\text{Si}_6\text{O}_{18})(\text{BO}_3)_3(\text{OH})_3\text{OH}$, a new mineral species of the tourmaline supergroup
591 from Grotta d’Oggi, San Pietro in Campo, island of Elba, Italy. American Mineralogist,
592 97, 989–994.
- 593 Bosi, F., Reznitskii, L.Z., and Sklyarov, E. V. (2013) Oxy-vanadium-dravite,
594 $\text{NaV}_3(\text{V}_4\text{Mg}_2)(\text{Si}_6\text{O}_{18})(\text{BO}_3)_3(\text{OH})_3\text{O}$: Crystal structure and redefinition of the
595 “vanadium-dravite” tourmaline. American Mineralogist, 98, 501–505.
- 596 Bosi, F., Reznitskii, L., Skogby, H., and Hålenius, U. (2014a) Vanadio-oxy-chromium-
597 dravite, $\text{NaV}_3(\text{Cr}_4\text{Mg}_2)(\text{Si}_6\text{O}_{18})(\text{BO}_3)_3(\text{OH})_3\text{O}$, a new mineral species of the tourmaline
598 supergroup. American Mineralogist, 99, 1155–1162.
- 599 Bosi, F., Skogby, H., Reznitskii, L., and Hålenius, U. (2014b) Vanadio-oxy-dravite,
600 $\text{NaV}_3(\text{Al}_4\text{Mg}_2)(\text{Si}_6\text{O}_{18})(\text{BO}_3)_3(\text{OH})_3\text{O}$, a new mineral species of the tourmaline
601 supergroup. American Mineralogist, 99, 218–224.
- 602 Bosi, F., Andreozzi, G.B., Agrosi, G., and Scandale, E. (2015) Fluor-tsilaisite,
603 $\text{NaMn}_3\text{Al}_6(\text{Si}_6\text{O}_{18})(\text{BO}_3)_3(\text{OH})_3\text{F}$, a new tourmaline from San Piero in Campo (Elba,
604 Italy) and new data on tsilaisitic tourmaline from the holotype specimen locality.
605 Mineralogical Magazine, 79, 89–101.
- 606 Bosi, F., Reznitskii, L., Hålenius, U., and Skogby, H. (2017) Crystal chemistry of Al-V-Cr
607 oxy-tourmalines from Sludyanka complex, Lake Baikal, Russia. European Journal of
608 Mineralogy, 29, 457–472.
- 609 Bosi, F., Skogby, H., and Hålenius, U. (2019) Thermally induced cation redistribution in
610 fluor-elbaite and Fe-bearing tourmalines. Physics and Chemistry of Minerals, 46, 371–
611 383.
- 612 Bosi, F., Pezzotta, F., Altieri, A., Andreozzi, G.B., Ballirano, P., and Tempesta, G. (2020)
613 Celleriite, IMA 2019-089, in: CNMNC Newsletter 53, European Journal of Mineralogy,
614 32.
- 615 Brown, I.D. (2006) The Chemical Bond in Inorganic Chemistry. Oxford University Press.
- 616 Burns, P.C., and Hawthorne, F.C. (1996) Static and dynamic Jahn-Teller effects in Cu^{2+}

- 617 oxysalt minerals. *Canadian Mineralogist*, 34, 1089–1105.
- 618 Burns, R.G., and Strens, R.G.J. (1967) Structural interpretation of polarized absorption
619 spectra of the Al-Fe-Mn-Cr epidotes. *Mineralogical Magazine and Journal of the*
620 *Mineralogical Society*, 36, 204–226.
- 621 Cámara, F., Ottolini, L., and Hawthorne, F.C. (2002) Crystal chemistry of three tourmalines
622 by SREF, EMPA, and SIMS. *American Mineralogist*, 87, 1437–1442.
- 623 Cempírek, J., Novák, M., Ertl, A., Hughes, J.M., Rossman, G.R., and Dyar, M.D. (2006) Fe-
624 bearing olenite with tetrahedrally coordinated Al from an abyssal pegmatite at Kutná
625 Hora, Czech Republic: Structure, crystal chemistry, optical and XANES spectra.
626 *Canadian Mineralogist*, 44, 23–30.
- 627 Cempírek, J., Houzar, S., Novák, M., Groat, L.A., Selway, J.B., and Šrein, V. (2013) Crystal
628 structure and compositional evolution of vanadium-rich oxy-dravite from graphite
629 quartzite at Bítoványky, Czech Republic. *Journal of Geosciences (Czech Republic)*, 58,
630 149–162.
- 631 Donnay, G.H., and Buerger, M.J. (1950) The determination of the crystal structure of
632 tourmaline. *Acta Crystallographica*, 3, 379–388.
- 633 Downs, R.T., and Hall-Wallace, M. (2003) The American Mineralogist Crystal Structure
634 Database. *American Mineralogist*, 88, 247–250.
- 635 Duchoslav, M., Marks, M.A.W., Drost, K., McCammon, C., Marschall, H.R., Wenzel, T., and
636 Markl, G. (2017) Changes in tourmaline composition during magmatic and hydrothermal
637 processes leading to tin-ore deposition: The Cornubian Batholith, SW England. *Ore*
638 *Geology Reviews*, 83, 215–234.
- 639 Dyar, M.D., Taylor, M.E., Lutz, T.M., Francis, C.A., Guidotti, C. V., and Wise, M. (1998)
640 Inclusive chemical characterization of tourmaline: Mössbauer study of Fe valence and
641 site occupancy. *American Mineralogist*, 83, 848–864.
- 642 Ertl, A., and Bačík, P. (2020) Considerations About Bi and Pb in the Crystal Structure of Cu-
643 Bearing Tourmaline. *Minerals*, 10, 706.
- 644 Ertl, A., and Tillmanns, E. (2012) The [9]-coordinated *X* site in the crystal structure of
645 tourmaline-group minerals. *Zeitschrift für Kristallographie*, 227, 456–459.
- 646 Ertl, A., Hughes, J.M., and Marler, B. (2001) Empirical formulae for the calculation of <*T-O*>

- 647 and X-O2 bond lengths in tourmaline and relations to tetrahedrally-coordinated boron.
648 Neues Jahrbuch für Mineralogie - Monatshefte, 2001, 548–557.
- 649 Ertl, A., Hughes, J.M., Pertlik, F., Foit, F.F., Wright, S.E., Brandstätter, F., and Marler, B.
650 (2002) Polyhedron distortions in tourmaline. Canadian Mineralogist, 40, 153–162.
- 651 Ertl, A., Hughes, J.M., Prowatke, S., Ludwig, T., Prasad, P.S.R., Brandstätter, F., Körner, W.,
652 Schuster, R., Pertlik, F., and Marschall, H. (2006) Tetrahedrally coordinated boron in
653 tourmalines from the liddicoatite-elbaite series from Madagascar: Structure, chemistry,
654 and infrared spectroscopic studies. American Mineralogist, 91, 1847–1856.
- 655 Ertl, A., Hughes, J.M., Prowatke, S., Ludwig, T., Brandstätter, F., Körner, W., and Dyar,
656 M.D. (2007) Tetrahedrally coordinated boron in Li-bearing olenite from “mushroom”
657 tourmaline from Momeik, Myanmar. Canadian Mineralogist, 45, 891–899.
- 658 Ertl, A., Mali, H., Schuster, R., Körner, W., Hughes, J.M., Brandstätter, F., and Tillmanns, E.
659 (2010a) Li-bearing, disordered Mg-rich tourmaline from a pegmatite-marble contact in
660 the Austroalpine basement units (Styria, Austria). Mineralogy and Petrology, 99, 89–
661 104.
- 662 Ertl, A., Marschall, H.R., Glester, G., Henry, D.J., Schertl, H.P., Ntaflos, T., Luvizotto, G.L.,
663 Nasdala, L., and Tillmanns, E. (2010b) Metamorphic ultrahigh-pressure tourmaline:
664 Structure, chemistry, and correlations to P-T conditions. American Mineralogist, 95, 1–
665 10.
- 666 Ertl, A., Rossman, G.R., Hughes, J.M., London, D., Wang, Y., O’Leary, J.A., Dyar, M.D.,
667 Prowatke, S., Ludwig, T., and Tillmanns, E. (2010c) Tourmaline of the elbaite-schorl
668 series from the Himalaya Mine, Mesa Grande, California: A detailed investigation.
669 American Mineralogist, 95, 24–40.
- 670 Ertl, A., Vereshchagin, O.S., Giester, G., Tillmanns, E., Meyer, H.-P.P., Ludwig, T.,
671 Rozhdestvenskaya, I. V., and Frank-Kamenetskaya, O. V. (2015) Structural and
672 chemical investigation of a zoned synthetic Cu-rich tourmaline. Canadian Mineralogist,
673 53, 209–220.
- 674 Ertl, A., Henry, D.J., and Tillmanns, E. (2018) Tetrahedral substitutions in tourmaline: a
675 review. European Journal of Mineralogy, 30, 465–470.
- 676 Faye, G.H. (1968) The optical absorption spectra of iron in six-coordinate sites in chlorite,
677 biotite, phlogopite and vivianite: some aspects of pleochroism in the sheet silicates.

- 678 Canadian Mineralogist, 9, 403–425.
- 679 Foit, F.F. (1989) Crystal chemistry of alkali-deficient schorl and tourmaline structural
680 relationships. American Mineralogist, 74, 422–431.
- 681 Foit, F.F., and Rosenberg, P.E. (1979) The structure of vanadium-bearing tourmaline and its
682 implications regarding tourmaline solid solutions. American Mineralogist, 64, 788–798.
- 683 Fridrichová, J., Bačík, P., Ertl, A., Wildner, M., Dekan, J., and Miglierini, M. (2018) Jahn-
684 Teller distortion of Mn³⁺-occupied octahedra in red beryl from Utah indicated by optical
685 spectroscopy. Journal of Molecular Structure, 1152, 79–86.
- 686 Gagné, O.C., and Hawthorne, F.C. (2015) Comprehensive derivation of bond-valence
687 parameters for ion pairs involving oxygen. Acta Crystallographica Section B: Structural
688 Science, Crystal Engineering and Materials, 71, 562–578.
- 689 Gatta, G.D., Bosi, F., McIntyre, G.J., and Skogby, H. (2014) First accurate location of two
690 proton sites in tourmaline: A single-crystal neutron diffraction study of oxy-dravite.
691 Mineralogical Magazine, 78, 681–692.
- 692 Grew, E.S., Barbier, J., Britten, J., Hålenius, U., and Shearer, C.K. (2007) The crystal
693 chemistry of welshite, a non-centrosymmetric (*P*1) aenigmatite-sapphirine-surinamite
694 group mineral. American Mineralogist, 92, 80–90.
- 695 Grew, E.S., Hålenius, U., Pasero, M., and Barbier, J. (2008) Recommended nomenclature for
696 the sapphirine and surinamite groups (sapphirine supergroup). Mineralogical Magazine,
697 72, 839–876.
- 698 Grice, J.D., and Ercit, T.S. (1993) Ordering of Fe and Mg in the tourmaline crystal structure:
699 The correct formula. Neues Jahrbuch für Mineralogie - Abhandlungen, 165, 245–266.
- 700 Grice, J.D., Ercit, T.S., and Hawthorne, F.C. (1993) Povondraite, a redefinition of the
701 tourmaline ferridravite. American Mineralogist, 78, 433–436.
- 702 Hawthorne, F.C. (1996) Structural mechanisms for light-element variations in tourmaline.
703 The Canadian Mineralogist, 34, 123–132.
- 704 ——— (2002) Bond-valence constraints on the chemical composition of tourmaline.
705 Canadian Mineralogist, 40, 789–797.
- 706 ——— (2016) Short-range atomic arrangements in minerals. I: The minerals of the
707 amphibole, tourmaline and pyroxene supergroups. European Journal of Mineralogy, 28,

- 708 513–536.
- 709 Hawthorne, F.C., MacDonald, D.J., and Burns, P.C. (1993) Reassignment of cation site
710 occupancies in tourmaline: Al-Mg disorder in the crystal structure of dravite. American
711 Mineralogist, 78, 265–270.
- 712 Hazarika, P., Upadhyay, D., and Pruseth, K.L. (2017) Episodic tourmaline growth and re-
713 equilibration in mica pegmatite from the Bihar Mica Belt, India: Major- and trace-
714 element variations under pegmatitic and hydrothermal conditions. Geological Magazine,
715 154, 68–86.
- 716 Henry, D.J., and Dutrow, B.L. (1996) Metamorphic Tourmaline and Its Petrologic
717 Applications. Reviews in Mineralogy, 33, 503–557.
- 718 Henry, D.J., and Dutrow, B.L. (2001) Compositional zoning and element partitioning in
719 nickeloan tourmaline from a metamorphosed karstbauxite from Samos, Greece.
720 American Mineralogist, 86, 1130–1142.
- 721 Henry, D.J., and Dutrow, B.L. (2012) Tourmaline at diagenetic to low-grade metamorphic
722 conditions: Its petrologic applicability. Lithos, 154, 16–32.
- 723 ——— (2018) Tourmaline studies through time: Contributions to scientific advancements.
724 Journal of Geosciences (Czech Republic), 63, 77–98.
- 725 Henry, D.J., Novák, M., Hawthorne, F.C., Ertl, A., Dutrow, B.L., Uher, P., and Pezzotta, F.
726 (2011) Nomenclature of the tourmaline-supergroup minerals. American Mineralogist, 96,
727 895–913.
- 728 Hong, W., Cooke, D.R., Zhang, L., Fox, N., and Thompson, J. (2017) Tourmaline-rich
729 features in the Heemskirk and Pieman Heads granites from western Tasmania, Australia:
730 Characteristics, origins, and implications for tin mineralization. American Mineralogist,
731 102, 876–899.
- 732 Hughes, J.M., Ertl, A., Dyar, M.D., Grew, E.S., Shearer, C.K., Yates, M.G., and Guidotti, C.
733 V. (2000) Tetrahedrally coordinated boron in a tourmaline: Boron-rich olenite from
734 Stoffhutte, Koralpe, Austria. Canadian Mineralogist, 38, 861–868.
- 735 Ito, J., and Hafner, S.S. (1974) Synthesis and study of gadolinites. American Mineralogist, 59,
736 700–708.
- 737 Jahn, H.A., Teller, E., and Donnan, F.G. (1937) Stability of polyatomic molecules in

- 738 degenerate electronic states - I—Orbital degeneracy. Proceedings of the Royal Society of
739 London. Series A - Mathematical and Physical Sciences, 161, 220–235.
- 740 Jiang, S.Y., Han, F., Shen, J.Z., and Palmer, M.R. (1999) Chemical and Rb-Sr, Sm-Nd
741 isotopic systematics of tourmaline from the Dachang Sn-polymetallic ore deposit,
742 Guangxi Province, P.R. China. *Chemical Geology*, 157, 49–67.
- 743 Johnson, M.L., Wentzell, C.Y., and Elen, S. (1997) Multicolored bismuth-bearing tourmaline
744 from Lundazi, Zambia. *Gems and Gemology*, 33, 204–211.
- 745 Kalliomäki, H., Wagner, T., Fusswinkel, T., and Sakellaris, G. (2017) Major and trace
746 element geochemistry of tourmalines from Archean orogenic gold deposits: Proxies for
747 the origin of gold mineralizing fluids? *Ore Geology Reviews*, 91, 906–927.
- 748 Kalt, A., Schreyer, W., Ludwig, T., Prowatke, S., Bernhardt, H.-J., and Ertl, A. (2001)
749 Complete solid solution between magnesian schorl and lithian excess-boron olenite in a
750 pegmatite from the Koralpe (eastern Alps, Austria). *European Journal of Mineralogy*, 13,
751 1191–1205.
- 752 Keller, P., Roda Robles, E., Pesquera Pérez, A., and Fontan, F. (1999) Chemistry, paragenesis
753 and significance of tourmaline in pegmatites of the Southern Tin Belt, central Namibia.
754 *Chemical Geology*, 158, 203–225.
- 755 Kubernátová, M., and Cempírek, J. (2019) Crystal chemistry of Pb-rich tourmaline from
756 pegmatite in Minh Tien, Vietnam. In 9th European Conference on Mineralogy and
757 Spectroscopy, Book of Abstracts.
- 758 Kutzschbach, M., Wunder, B., Rhede, D., Koch-Müller, M., Ertl, A., Giester, G., Heinrich,
759 W., and Franz, G. (2016) Tetrahedral boron in natural and synthetic HP/UHP tourmaline:
760 Evidence from Raman spectroscopy, EMPA, and single-crystal XRD. *American
761 Mineralogist*, 101, 93–104.
- 762 Lussier, A.J., Aguiar, P.M., Michaelis, V.K., Kroeker, S., Herwig, S., Abdu, Y., and
763 Hawthorne, F.C. (2008) Mushroom elbaite from the Kat Chay mine, Momeik, near
764 Mogok, Myanmar: I. Crystal chemistry by SREF, EMPA, MAS NMR and Mössbauer
765 spectroscopy. *Mineralogical Magazine*, 72, 747–761.
- 766 Lussier, A.J., Ball, N.A., Hawthorne, F.C., Henry, D.J., Shimizu, R., Ogasawara, Y., and Ota,
767 T. (2016) Maruyamaite, $K(MgAl_2)(Al_5Mg)Si_6O_{18}(BO_3)_3(OH)_3O$, a potassium-dominant
768 tourmaline from the ultrahigh-pressure Kokchetav massif, northern Kazakhstan:

- 769 Description and crystal structure. *American Mineralogist*, 101, 355–361.
- 770 MacDonald, D.J., and Hawthorne, F.C. (1995) The crystal chemistry of Si \leftrightarrow Al substitution
771 in tourmaline. *The Canadian Mineralogist*, 33, 849–858.
- 772 Marschall, H.R., Ertl, A., Hughes, J.M., and McCammon, C. (2004) Metamorphic Na- and
773 OH-rich disordered dravite with tetrahedral boron, associated with omphacite, from
774 Syros, Greece: chemistry and structure. *European Journal of Mineralogy*, 16, 817–823.
- 775 Nishio-Hamane, D., Minakawa, T., Yamaura, J.I., Oyama, T., Ohnishi, M., and
776 Shimobayashi, N. (2014) Adachiite, a Si-poor member of the tourmaline supergroup
777 from the Kiura mine, Oita Prefecture, Japan. *Journal of Mineralogical and Petrological*
778 *Sciences*. Tohoku University.
- 779 Pieczka, A., Gołębiewska, B., Jeleń, P., Włodek, A., Szełęg, E., and Szuszkiewicz, A. (2018)
780 Towards zn-dominant tourmaline: A case of zn-rich fluor-elbaite and elbaite from the
781 julianna system at Piława Górna, Lower Silesia, SW Poland. *Minerals*.
- 782 Reznitskii, L., Clark, C.M., Hawthorne, F.C., Grice, J.D., Skogby, H., Hålenius, U., and Bosi,
783 F. (2014) Chromo-alumino-povondraite, $\text{NaCr}_3(\text{Al}_4\text{Mg}_2)(\text{Si}_6\text{O}_{18})(\text{BO}_3)_3(\text{OH})_3\text{O}$, a new
784 mineral species of the tourmaline supergroup. *American Mineralogist*, 99, 1767–1773.
- 785 Rumyantseva, E. V. (1983) Chromdravite, a new mineral. *Zapiski Vsesoyuznogo*
786 *Mineralogicheskogo Obshchestva*, 112, 222–226.
- 787 Selway, J.B., Novák, M., Černý, P., and Hawthorne, F.C. (1999) Compositional evolution of
788 tourmaline in lepidolite-subtype pegmatites. *European Journal of Mineralogy*.
- 789 Selway, J.B., Cerny, P., Hawthorne, F.C., and Novak, M. (2000) The Tanco pegmatite at
790 Bernic Lake, Manitoba. XIV. Internal tourmaline. *Canadian Mineralogist*, 38, 877–891.
- 791 Shannon, R.D. (1976) Revised effective ionic radii and systematic studies of interatomic
792 distances in halides and chalcogenides. *Acta Crystallographica Section A*, 32, 751–767.
- 793 Van Hinsberg, V.J. (2011) Preliminary experimental data on trace-element partitioning
794 between tourmaline and silicate melt. *Canadian Mineralogist*, 49, 153–163.
- 795 Van Hinsberg, V.J., Franz, G., and Wood, B.J. (2017) Determining subduction-zone fluid
796 composition using a tourmaline mineral probe. *Geochemical Perspectives Letters*, 3,
797 160–169.
- 798 Vereshchagin, O.S., Rozhdestvenskaya, I. V., Frank-Kamenetskaya, O. V., Zolotarev, A.A.,

- 799 and Mashkovtsev, R.I. (2013) Crystal chemistry of Cu-bearing tourmalines. American
800 Mineralogist, 98, 1610–1616.
- 801 Vezzoni, S., Biagioni, C., D’Orazio, M., Pieruccioni, D., Galanti, Y., Petrelli, M., and Molli,
802 G. (2018) Evidence of Permian magmatism in the Alpi Apuane metamorphic complex
803 (Northern Apennines, Italy): New hints for the geological evolution of the basement of
804 the Adria plate. *Lithos*, 318–319, 104–123.
- 805 Williamson, B.J., Spratt, J., Adams, J.T., Tindle, A.G., and Stanley, C.J. (2000) Geochemical
806 constraints from zoned hydrothermal tourmalines on fluid evolution and Sn
807 mineralization: An example from fault breccias at Roche, SW England. *Journal of*
808 *Petrology*, 41, 1439–1453.
- 809 Yu, J.M., and Jiang, S.Y. (2003) Chemical composition of tourmaline from the Yunlong tin
810 deposit, Yunnan, China: Implications for ore genesis and mineral exploration.
811 *Mineralogy and Petrology*, 77, 67–84.
- 812 Žáček, V., Frýda, J., Petrov, A., and Hyršl, J. (2000) Tourmalines of the povondraite -
813 (oxy)dravite series from the cap rock of meta-evaporite in Alto Chapare, Cochabamba,
814 Bolivia. *Journal of the Czech Geological Society*, 45, 3–12.
- 815
- 816

817 **Table 1.** Calculated bond lengths (in Å) of chemical elements at selected structural sites
 818 in tourmaline.

Bond	Bond length	Bond	Bond length	Bond	Bond length	Bond	Bond length
T site		Y and Z site		Y and Z site		X site	
Si ⁴⁺ -O	1.6240	Al ³⁺ -O	1.9043	Sn ⁴⁺ -O	2.0929	Na ⁺ -O	2.6178
B ³⁺ -O	1.4747	Si ⁴⁺ -O	1.7817	Ga ³⁺ -O	1.9751	Ca ²⁺ -O	2.5222
Be ²⁺ -O	1.6349	Be ²⁺ -O	1.7553	Sc ³⁺ -O	2.0933	K ⁺ -O	2.9215
Al ³⁺ -O	1.7462	Mg ²⁺ -O	2.0991	Cu ²⁺ -O	2.0806	Rb ⁺ -O	3.0433
Ti ⁴⁺ -O	1.8190	Fe ²⁺ -O	2.1536	Zn ²⁺ -O	2.1086	Cs ⁺ -O	3.1991
Fe ³⁺ -O	1.8696	Fe ³⁺ -O	2.0155	Ni ²⁺ -O	2.0737	Sr ²⁺ -O	2.6785
		Mn ²⁺ -O	2.2023	Zr ⁴⁺ -O	2.0776	Ba ²⁺ -O	2.8337
		Mn ³⁺ -O	1.9942	Pb ⁴⁺ -O*	2.3664	Pb ²⁺ -O*	2.6968
		Li ⁺ -O	2.2110	U ⁴⁺ -O	2.2512	U ⁴⁺ -O	2.4025
		Ti ⁴⁺ -O	1.9577	Th ⁴⁺ -O	2.2873	Th ⁴⁺ -O	2.4576
		Cr ³⁺ -O	1.9752	Ce ³⁺ -O	2.3836	Ce ³⁺ -O	2.5414
		V ³⁺ -O	2.0036	Y ³⁺ -O	2.2601	Y ³⁺ -O	2.4251
				Yb ³⁺ -O	2.2275	Yb ³⁺ -O	2.3788
				Ce ⁴⁺ -O	2.2147	Ce ⁴⁺ -O	2.3833
				Bi ⁵⁺ -O*	2.1389	Bi ³⁺ -O*	2.4954
				Bi ³⁺ -O*	2.3376		

819 * Data from (Ertl and Bačík 2020)

820

821 **Table 2.** Empirical bond lengths (in Å) of chemical elements at selected structural sites in
 822 tourmaline with the +10% and -10% deviation for the most typical occupant of the selected
 823 site determining the range of the “Goldilocks zone” for each site.

Bond	Bond length	+10%	-10%
^T Si ⁴⁺ -O	1.6206	1.4586	1.7827
^T B ³⁺ -O	1.4817		
^B B ³⁺ -O	1.3722	1.2350	1.5094
^Z Al ³⁺ -O	1.906*	1.7154	2.0966
^Y Mg ²⁺ -O	2.0304	1.8274	2.2335
^Y Fe ²⁺ -O	2.0421		
^Y Mn ²⁺ -O	2.1579		
^Y Li ⁺ -O	2.0902		
^X Na-O	2.6920	2.4228	2.9612
^X □-O	2.7258		
^X Ca ²⁺ -O	2.6091		
^X K ⁺ -O	2.6866		

824 * Data from (Bosi and Andreozzi 2013)

825

826

827 **Figure captions:**

828 **Figure 1.** One unit cell of the tourmaline crystal structure (Bačík et al. 2012) with
829 framework of ZO_6 octahedra enclosing structural islands with alternating T_6O_{18} tetrahedral
830 rings, triplets of YO_6 octahedra and BO_3 triangles.

831 **Figure 2.** Interconnected chains of ZO_6 octahedra oriented parallel to c forming 3D
832 framework.

833 **Figure 3.** Local environment of TO_4 tetrahedron in (a) polyhedral model and (b) as a
834 topological graph.

835 **Figure 4.** Local environment of BO_3 triangle in (a) polyhedral model and (b) as a
836 topological graph.

837 **Figure 5.** Local environment of ZO_6 octahedron in (a) polyhedral model and (b) as a
838 topological graph.

839 **Figure 6.** Local environment of YO_6 octahedron in (a) polyhedral model and (b) as a
840 topological graph.

841 **Figure 7.** Local environment of XO_4 trigonal antiprism in (a) polyhedral model, (b) as a
842 complete topological graph, topological graph of local environment in (c) $+c$ and (d) $-c$
843 direction.

844 **Figure 8.** Calculated bond lengths for each bond in the (a) tetrahedral T -site and (b)
845 triangular B -site coordination of cations. Horizontal dashed lines are for empirical bond
846 lengths at each site. The horizontal dotted line is the 10% deviation from the empirical bond
847 length. The “Goldilocks zone” is white. The substitution is significantly limited for cations in
848 the grey zone.

849 **Figure 9.** Calculated bond lengths for each bond in the octahedral Z - and Y -site
850 coordination of cations – (a) major and minor elements, (b) trace elements. Horizontal dashed
851 lines are for empirical bond lengths for each cation. The horizontal dotted line is the 10%
852 deviation from the empirical bond length. The “Goldilocks zone” is white. The substitution is
853 significantly limited for cations in the grey zone.

854 **Figure 10.** Calculated bond lengths for each bond in the 9-fold trigonal antiprismatic X -
855 site coordination of cations. Horizontal dashed lines are for empirical bond lengths for each
856 cation. The horizontal dotted line is the 10% deviation from the empirical bond length. The

857 “Goldilocks zone” is white. The substitution is significantly limited for cations in the grey
858 zone.

859 **Figure 11.** (a) Ideal octahedron with O anions; (b) the maximum size of cation in the
860 ideal octahedron is the square root of two squares of ligand ionic radius; (c) after the
861 subtraction of O²⁻ ionic radius the cation ionic radius is equal to 0.56 Å.

Fig 1

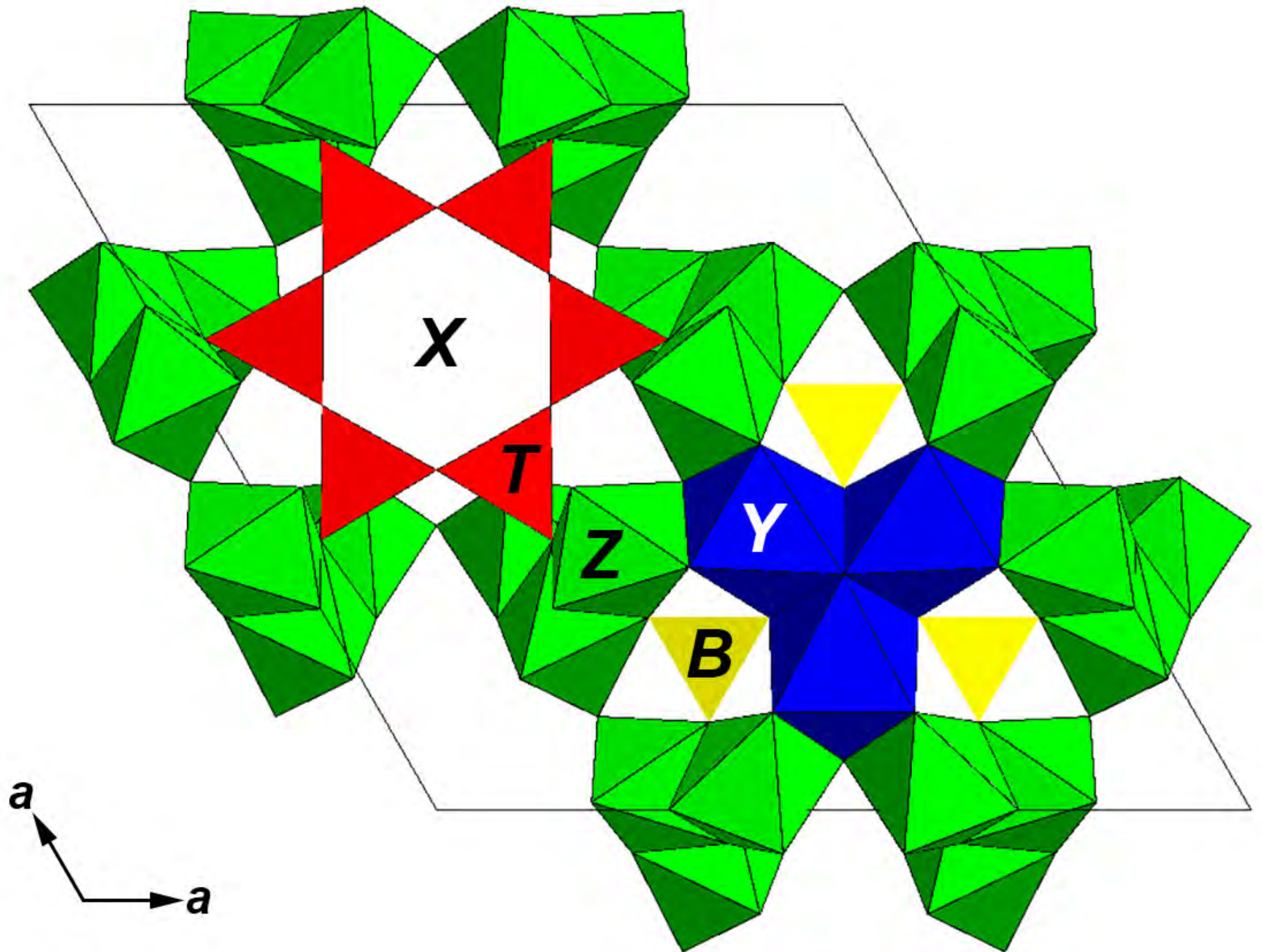


Fig. 2

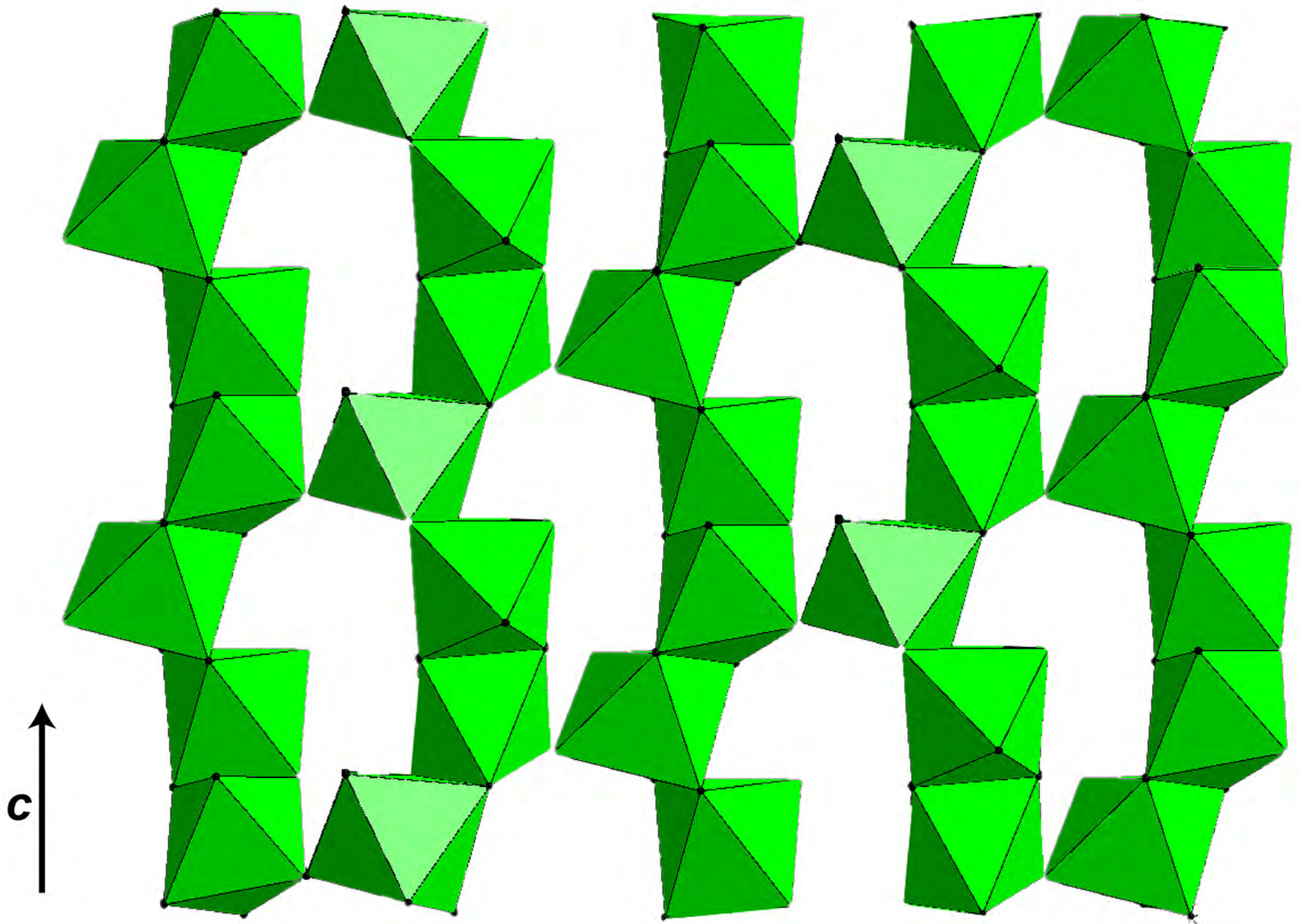


Fig. 3

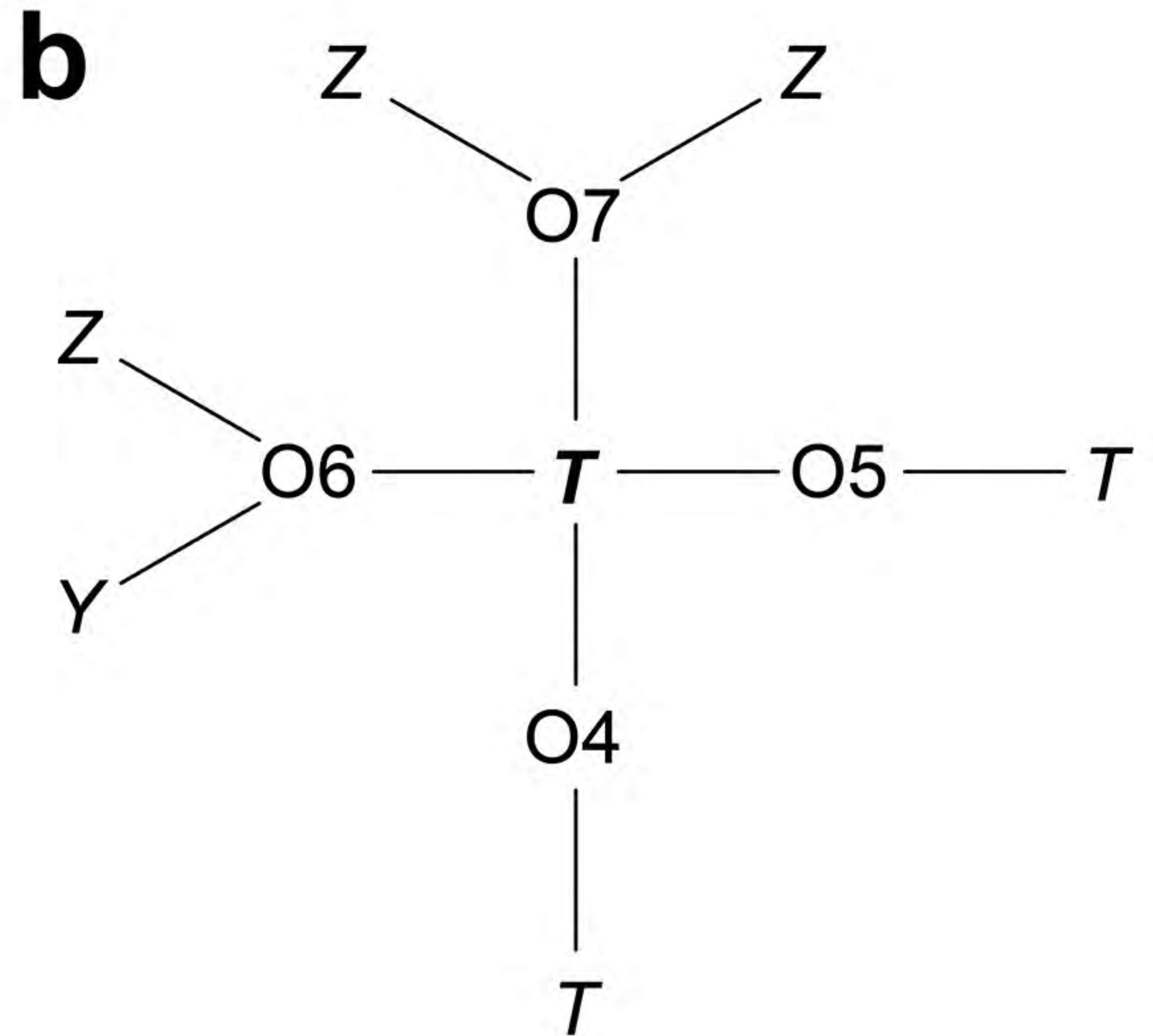
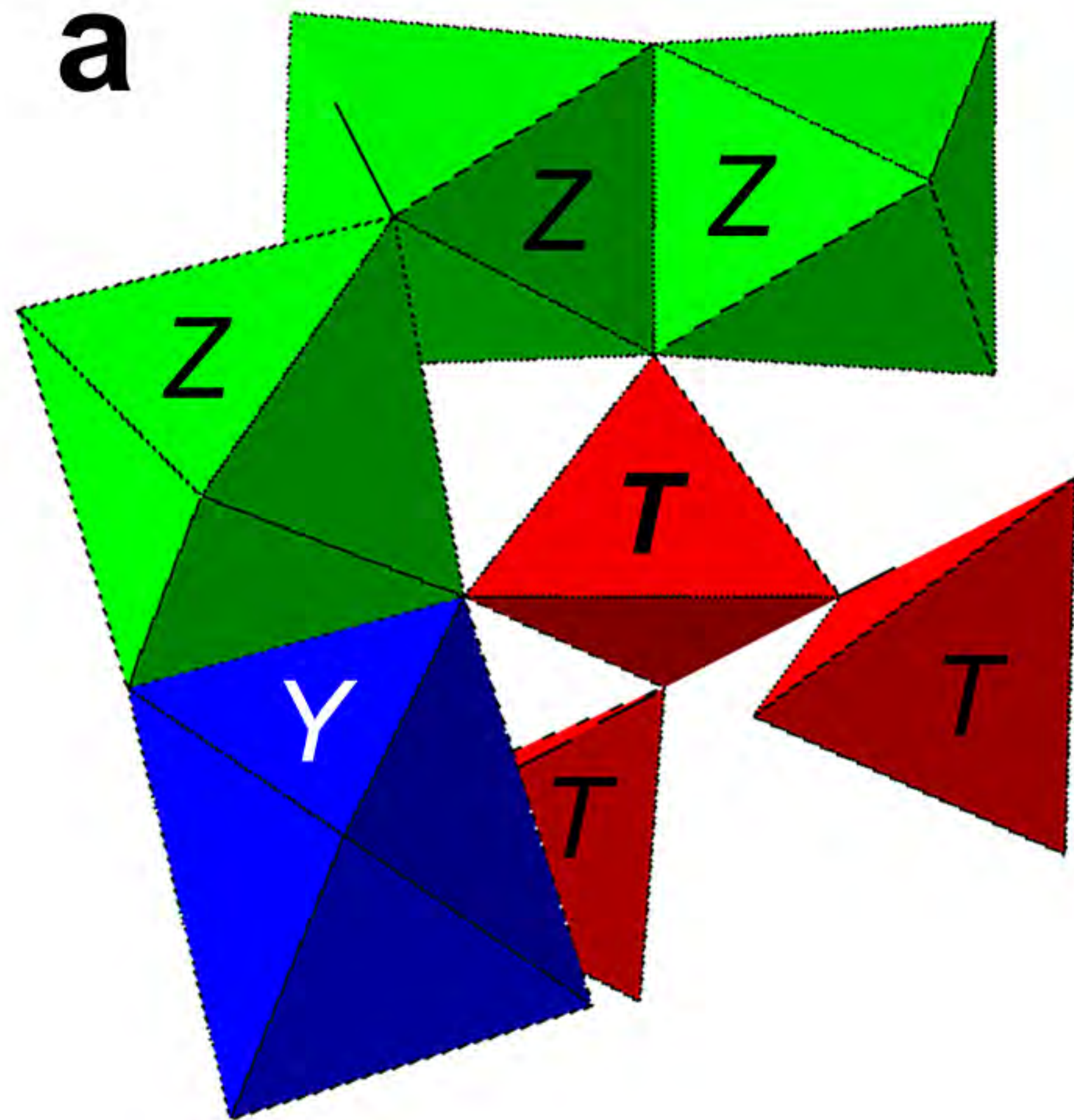
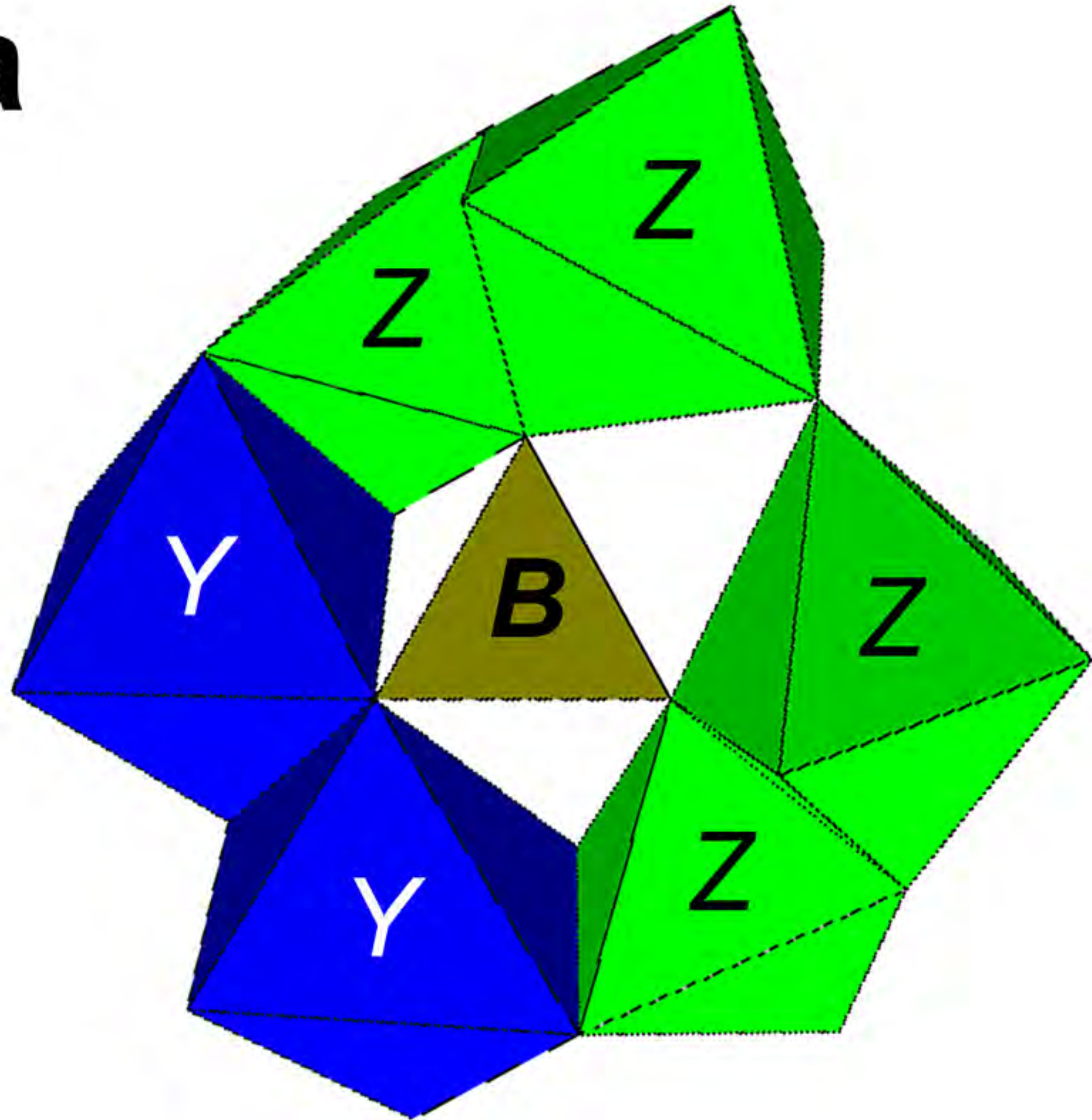


Fig. 4

a



b

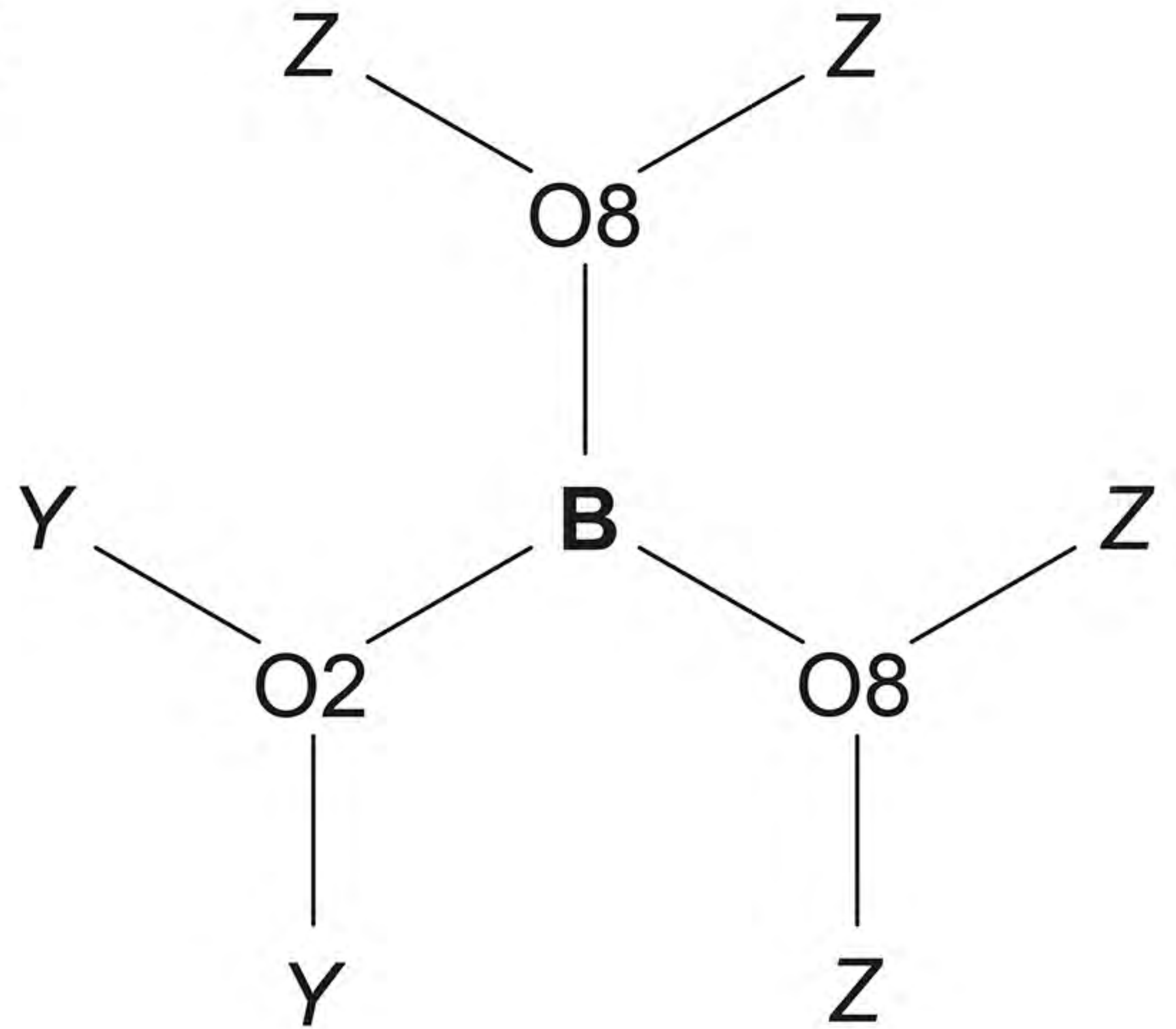
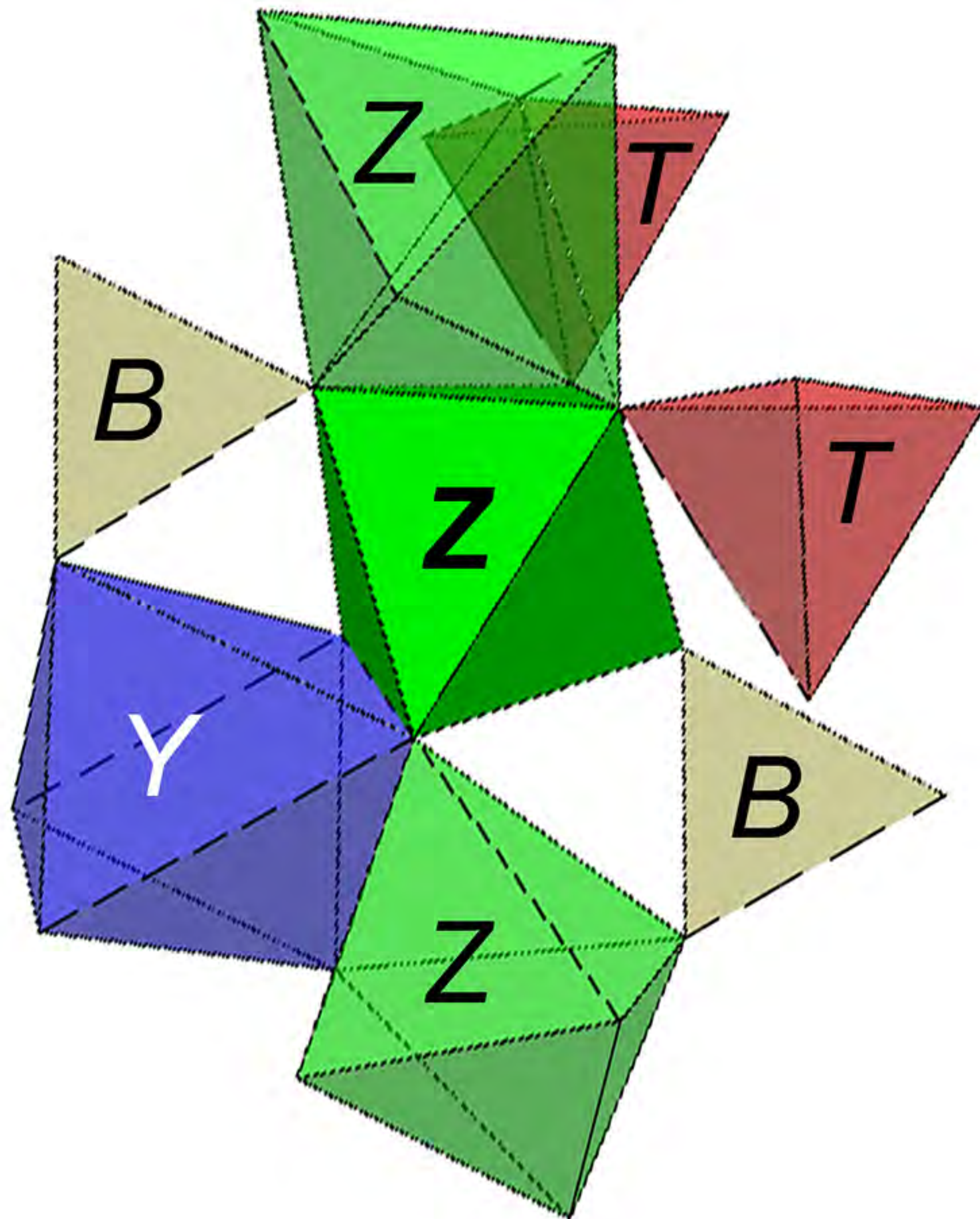


Fig. 5

a



b

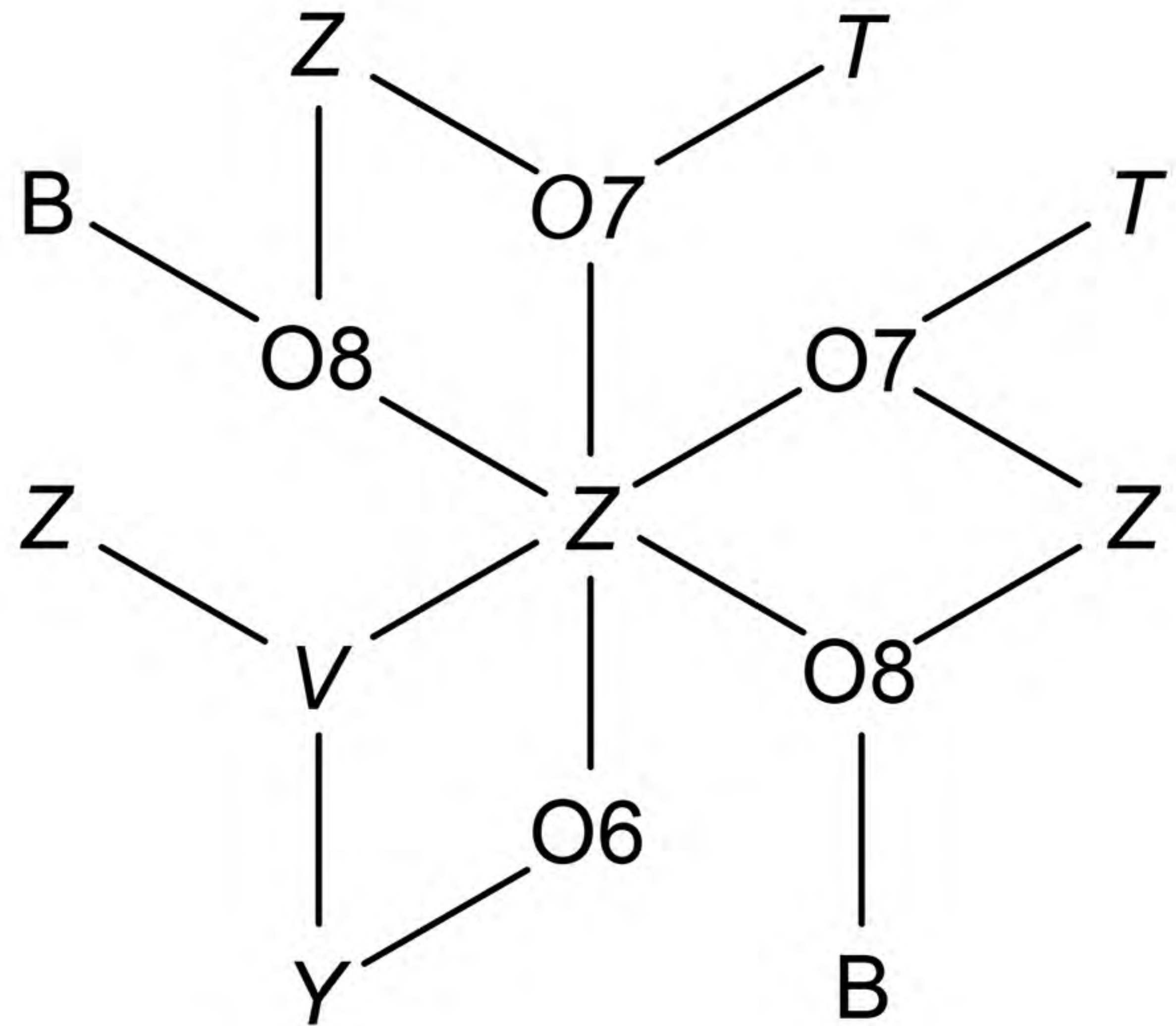
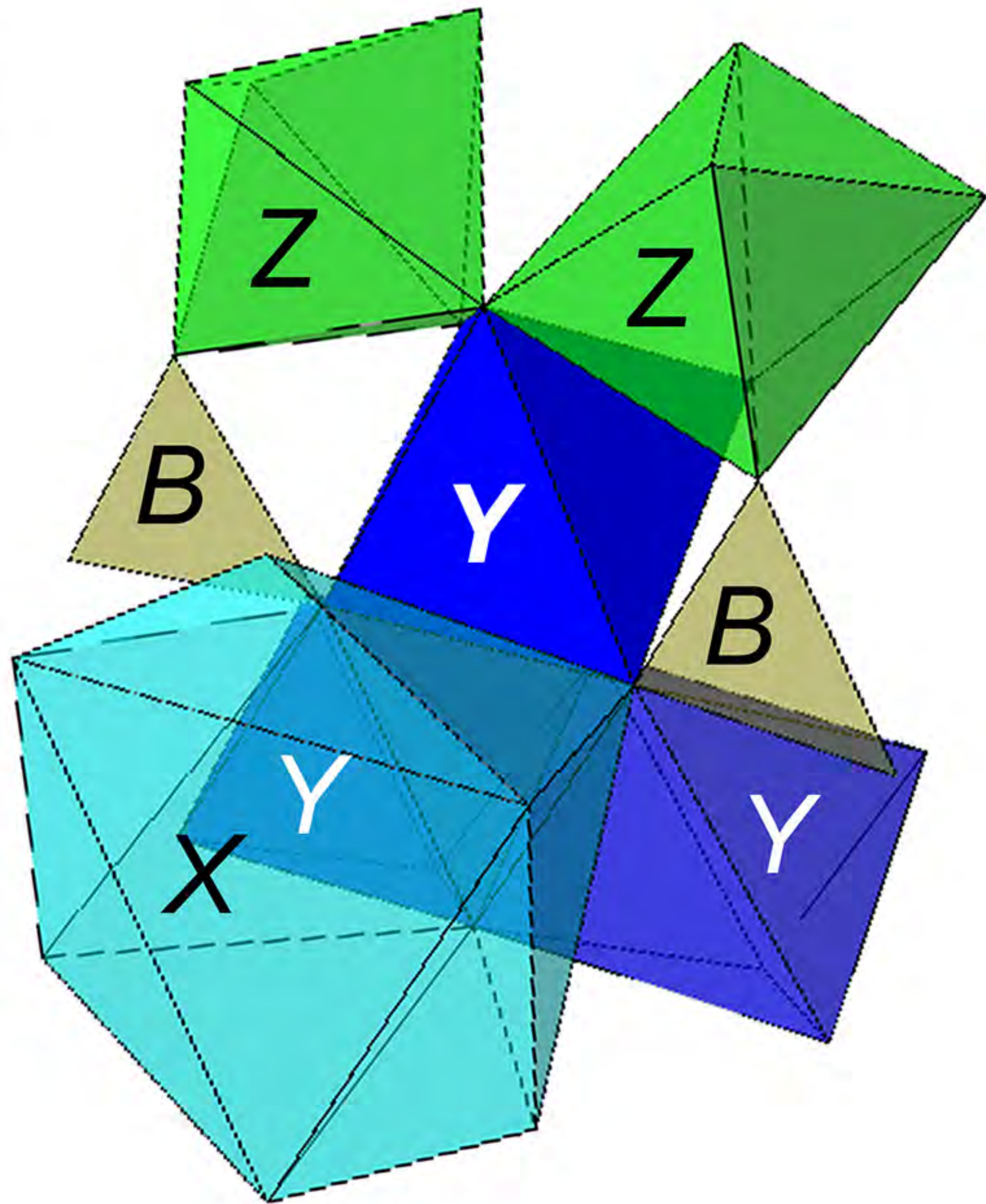


Fig. 6

a



b

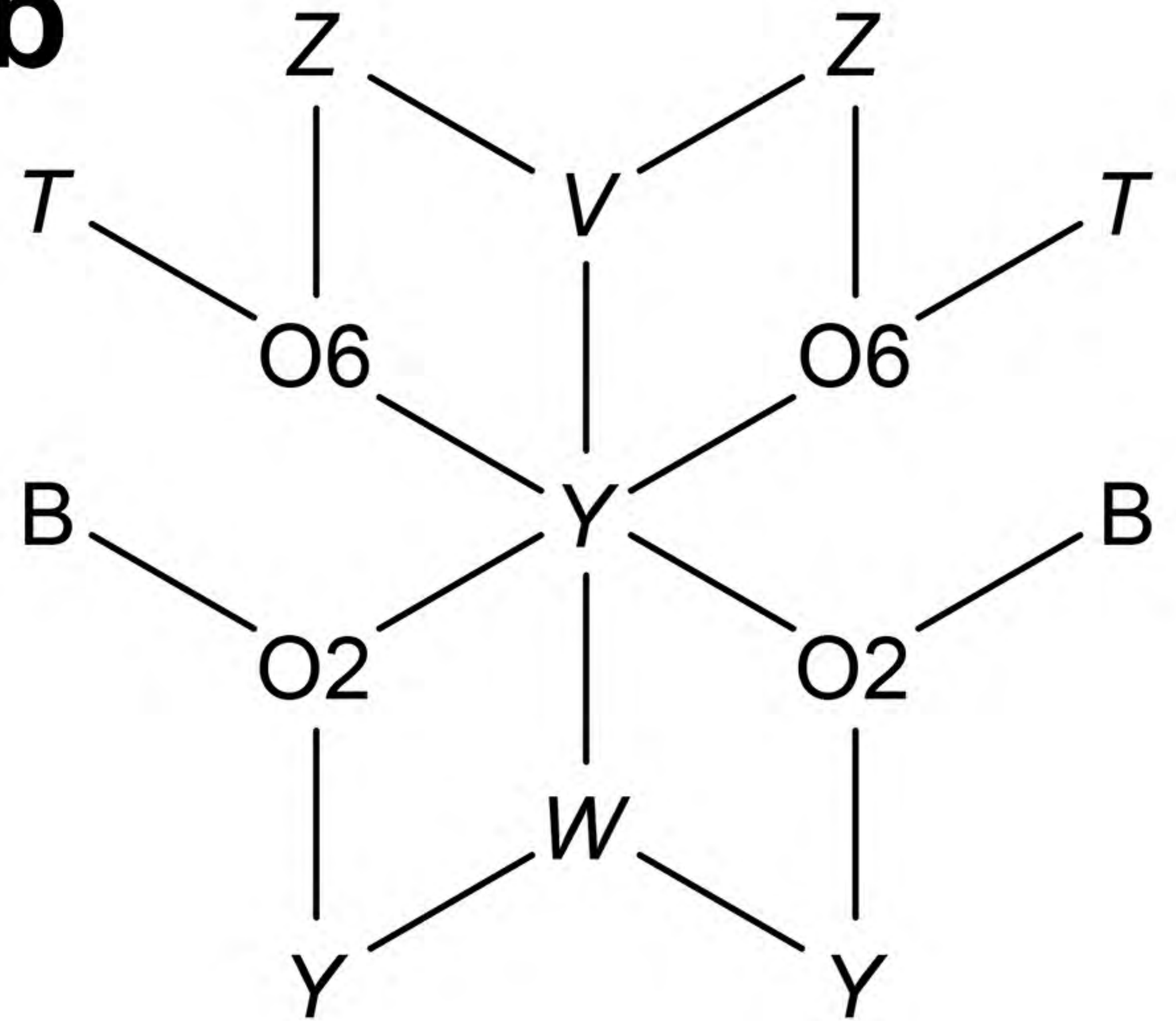
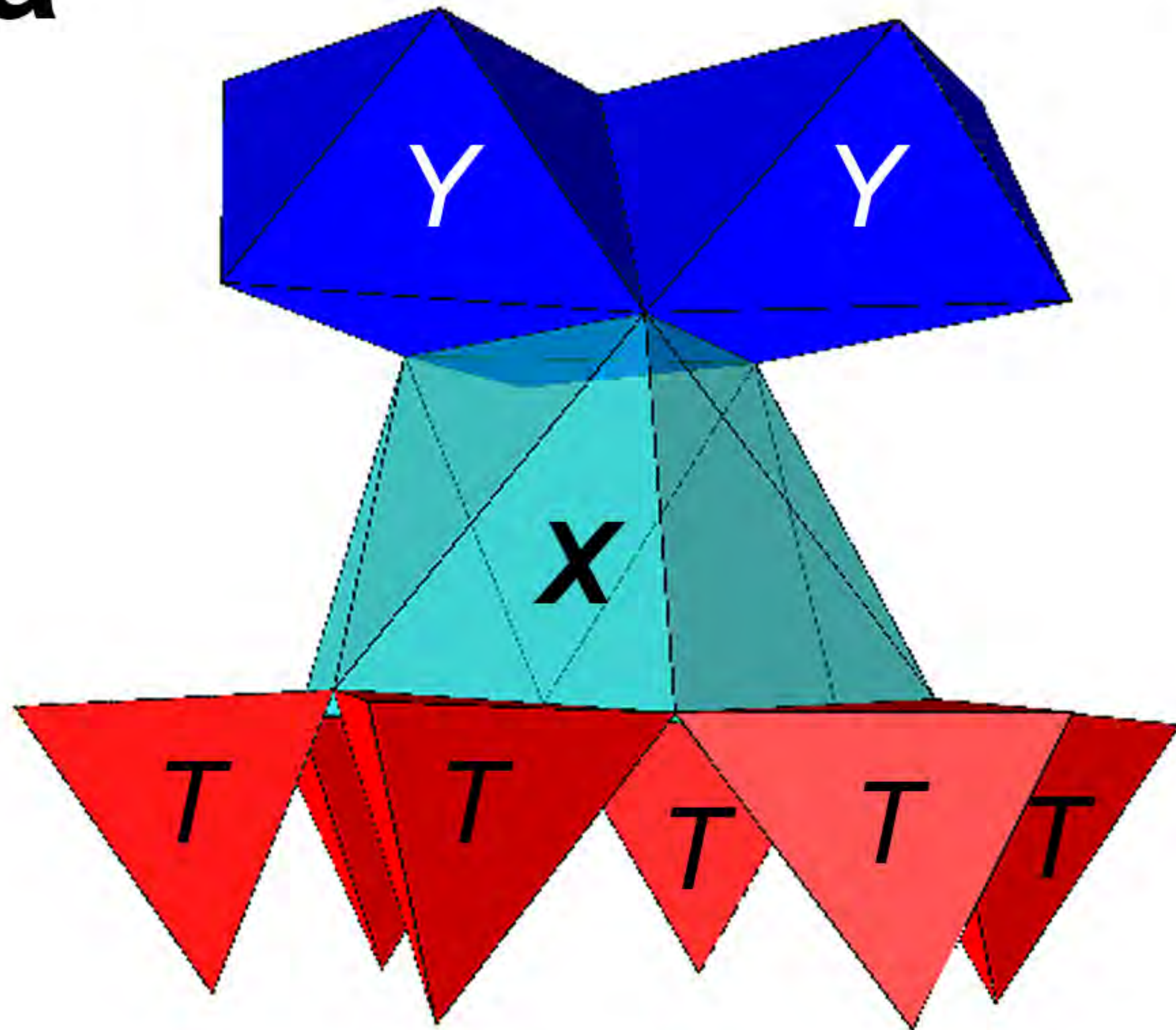
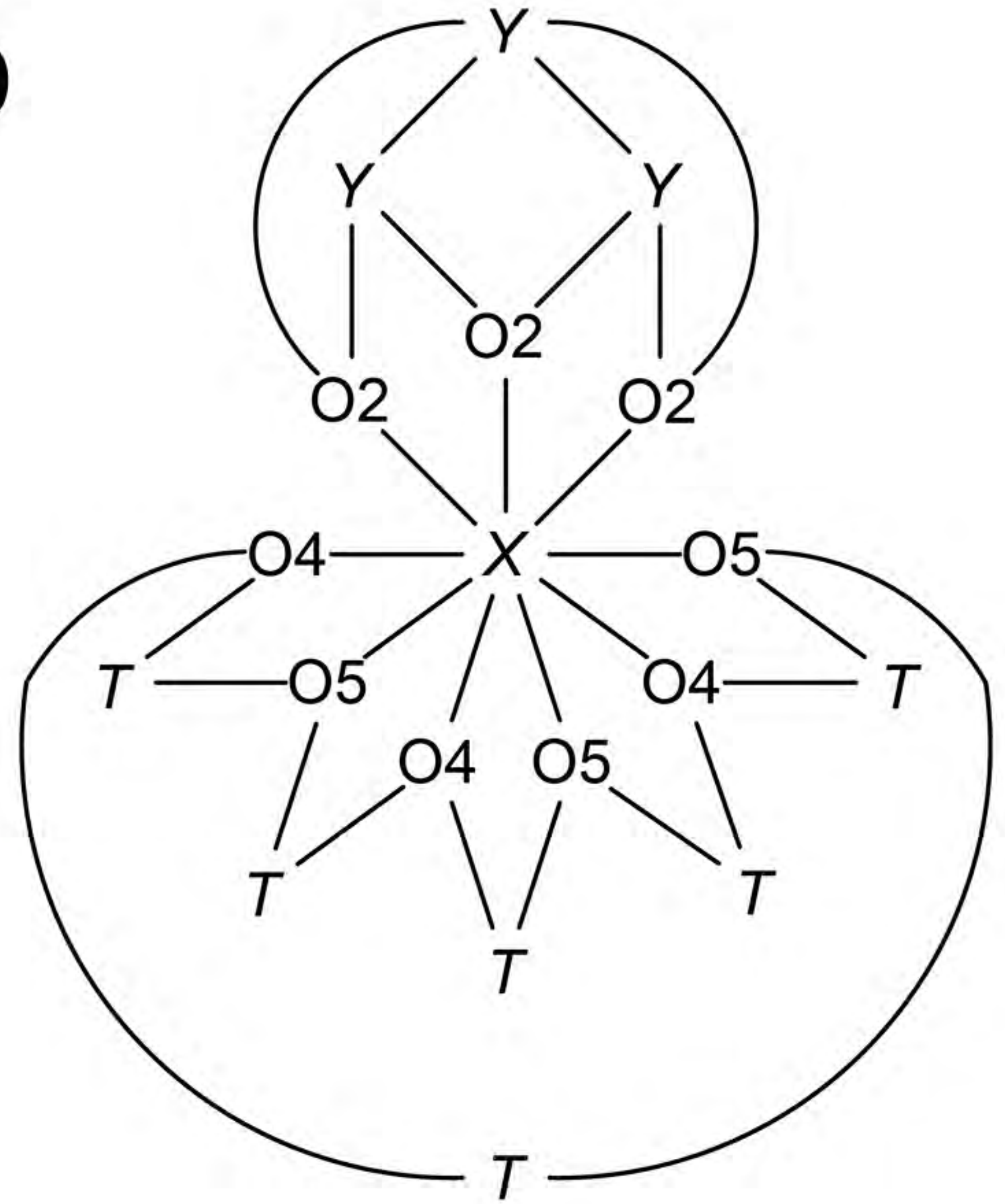


Fig. 7

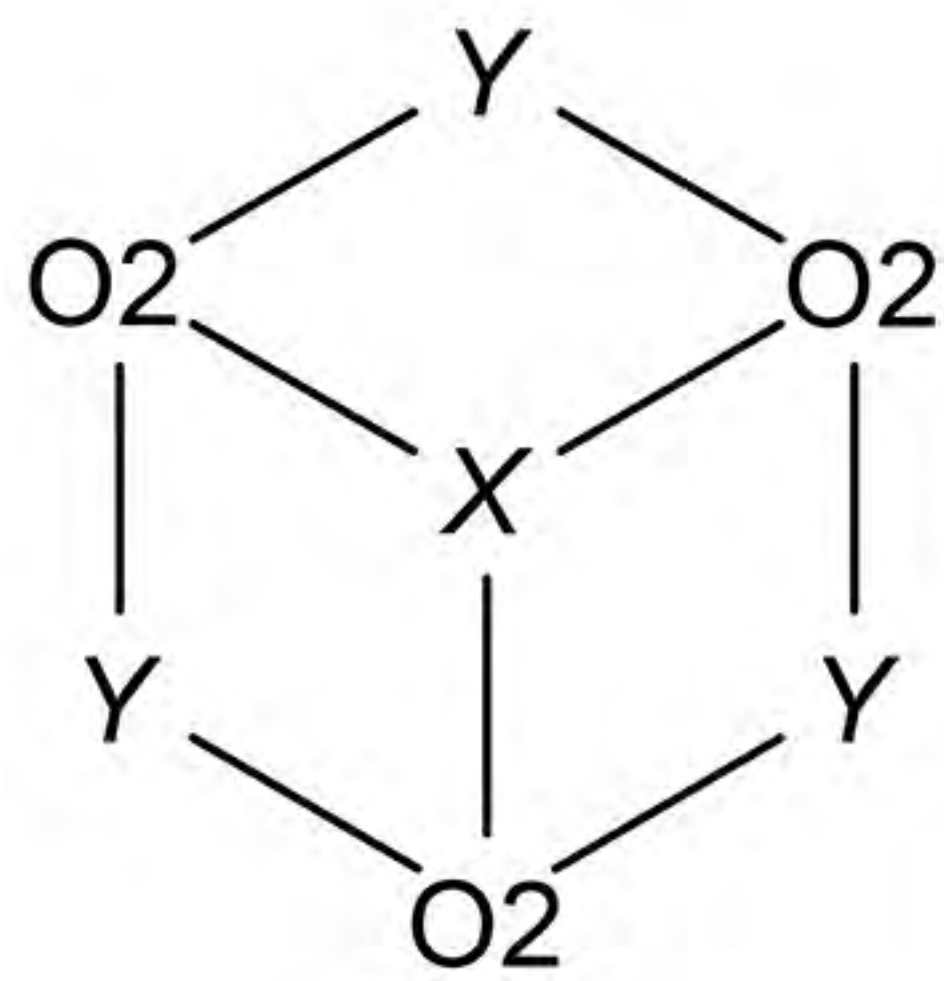
a



b



c



d

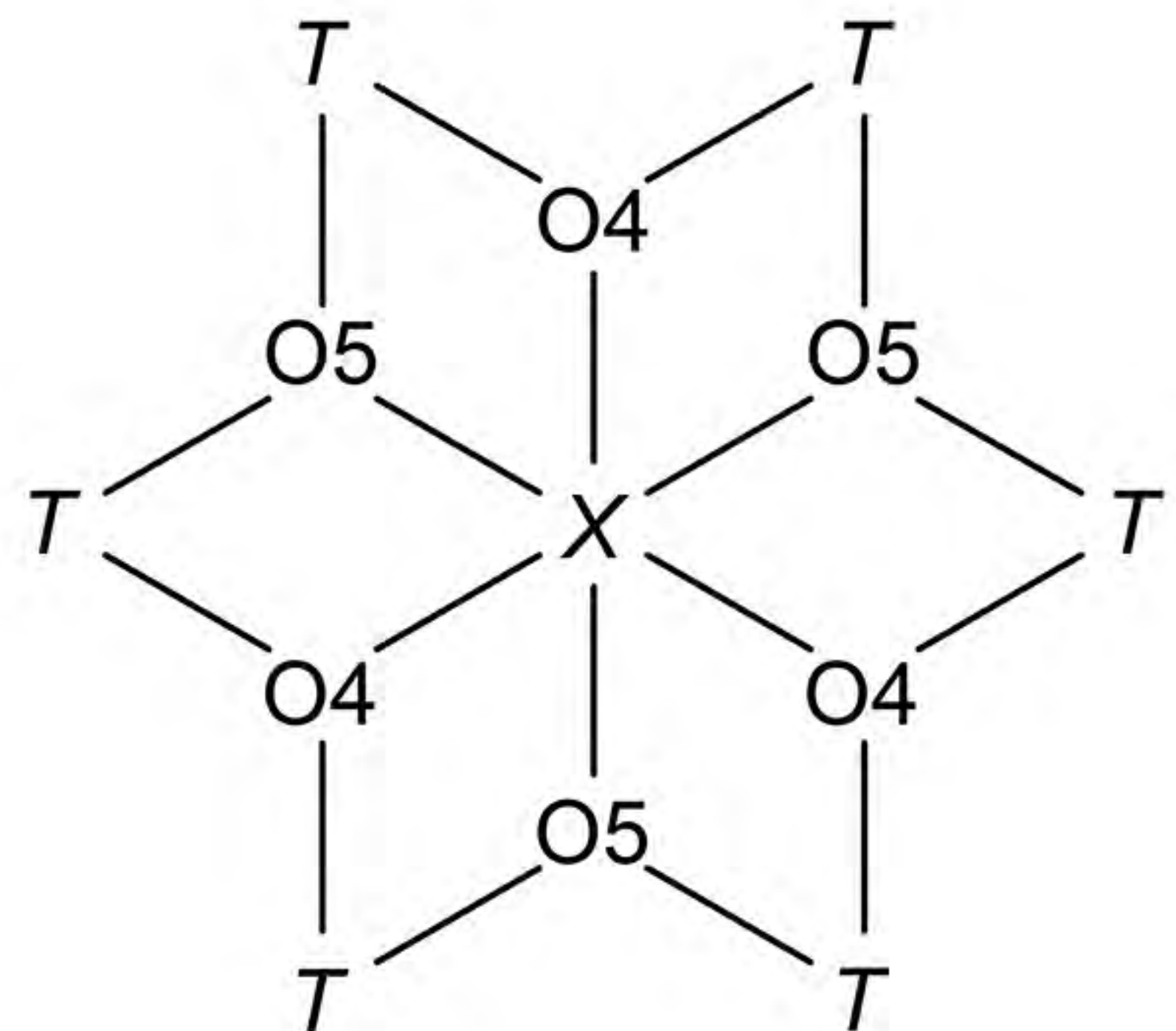


Fig. 8

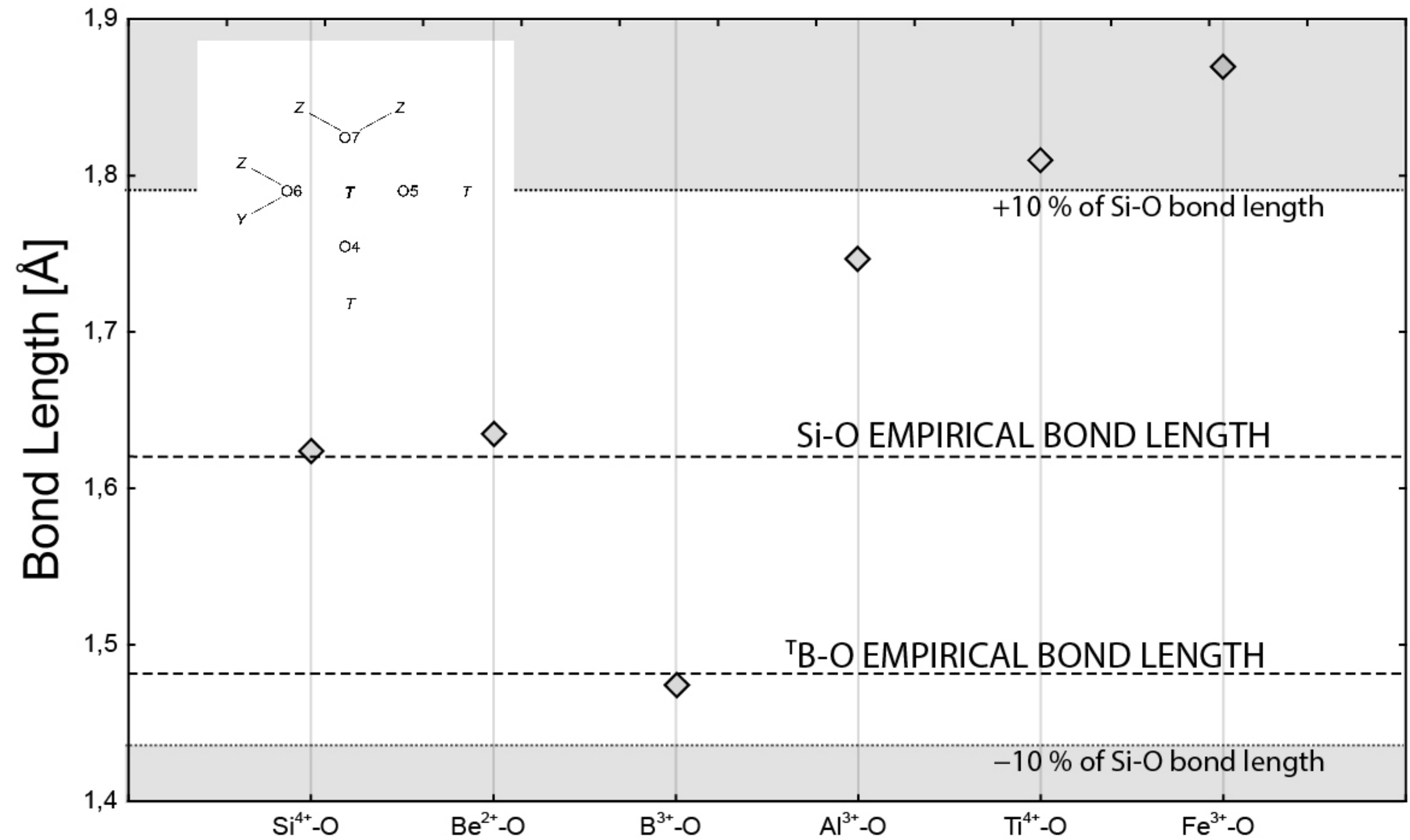


Fig. 9

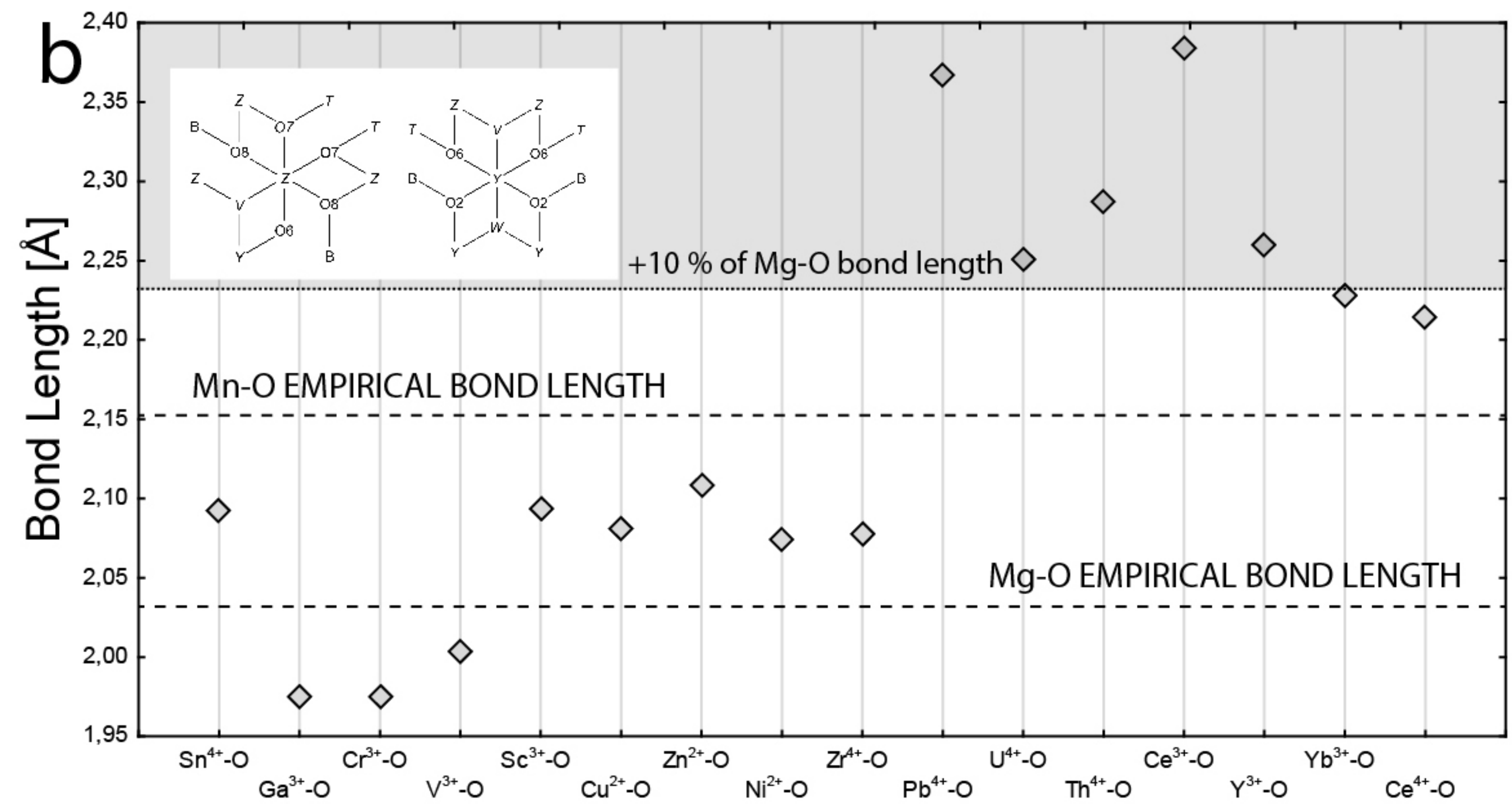
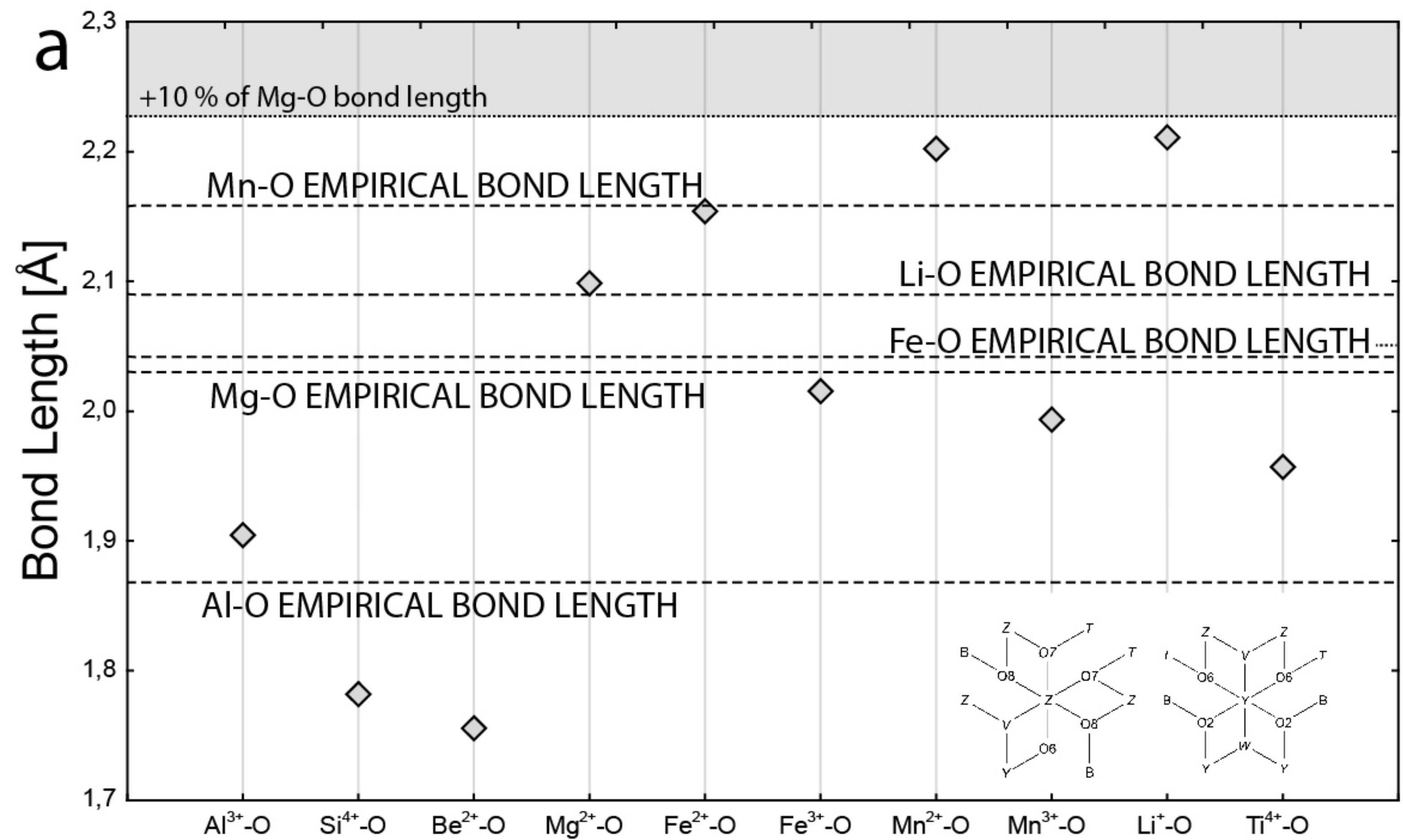


Fig. 10

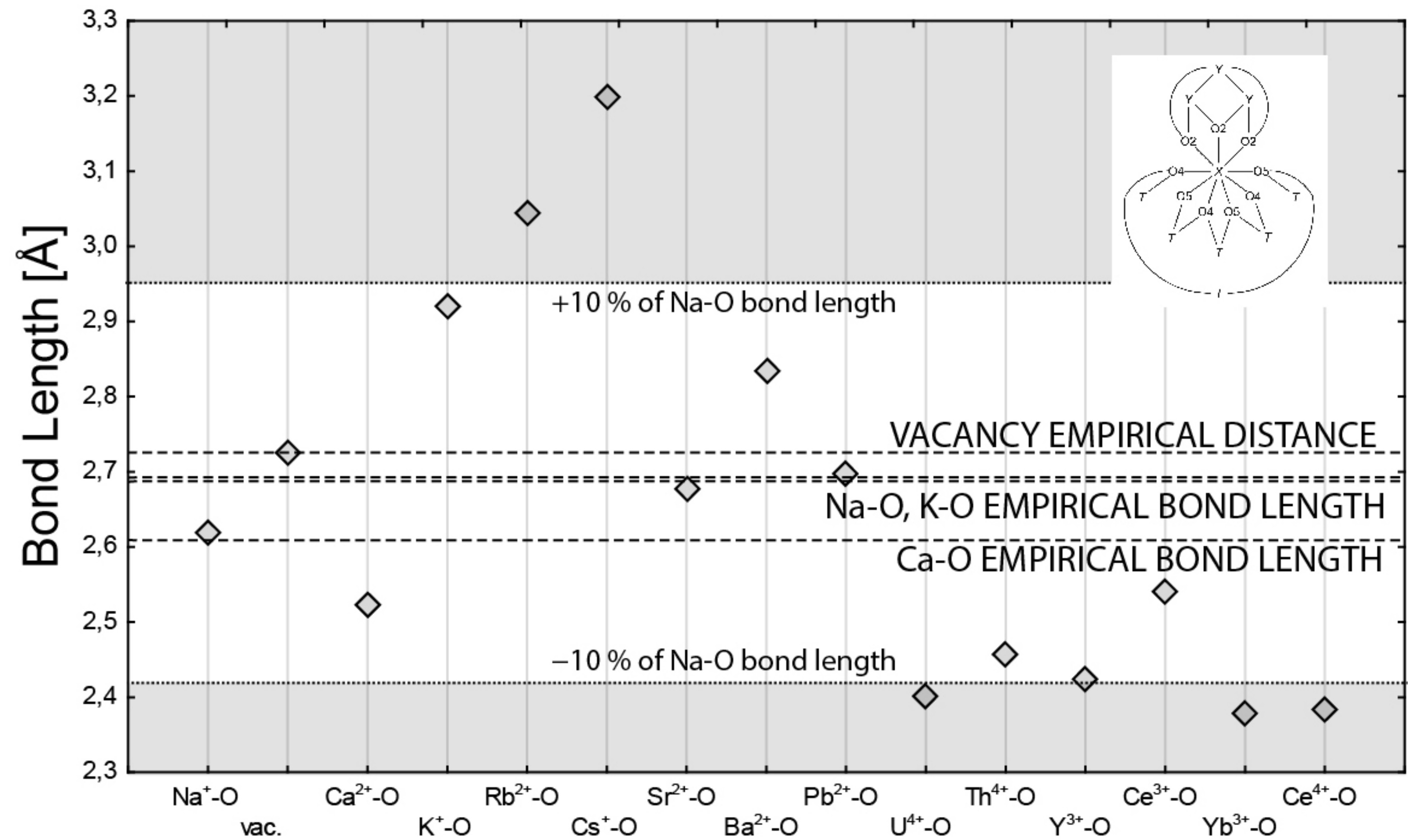
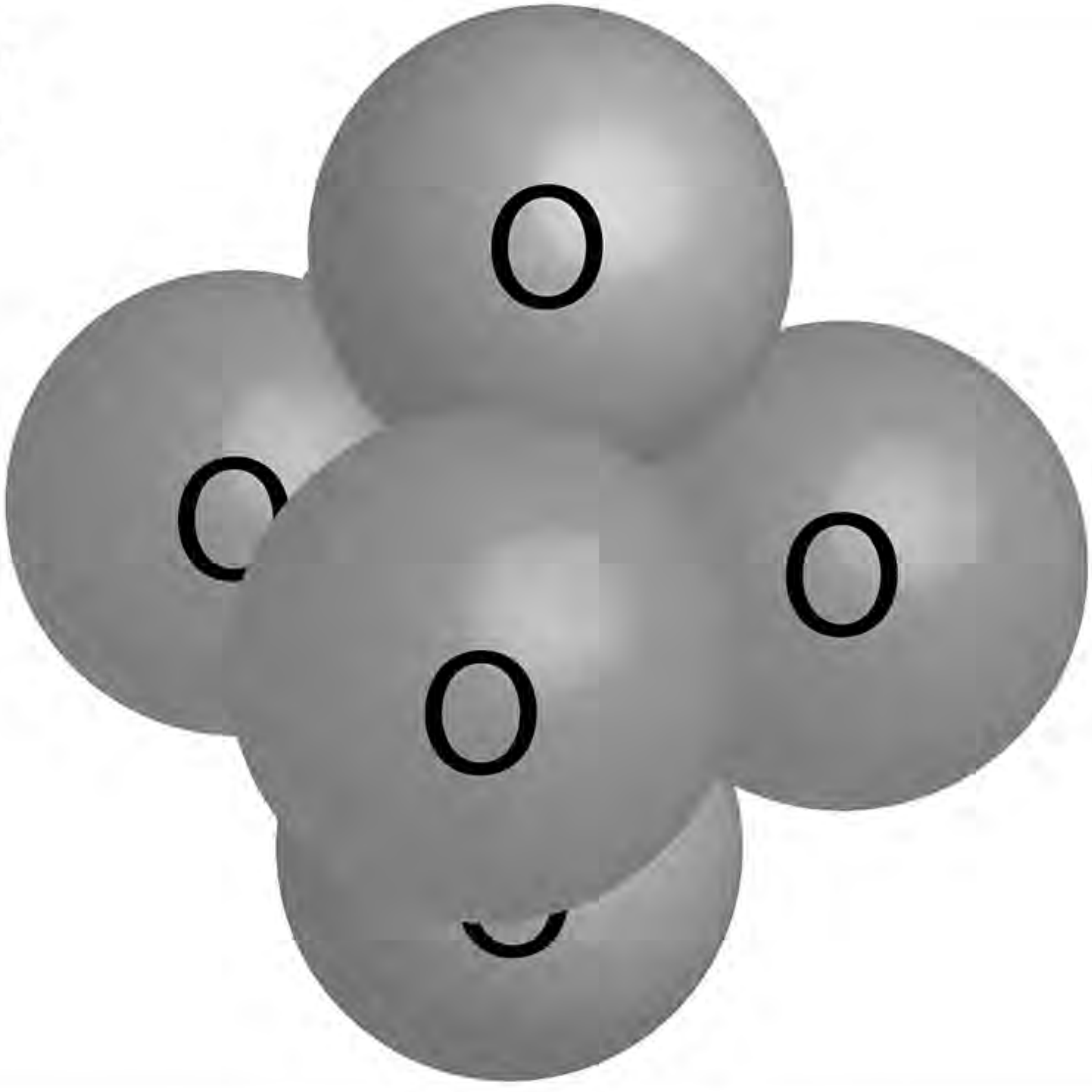
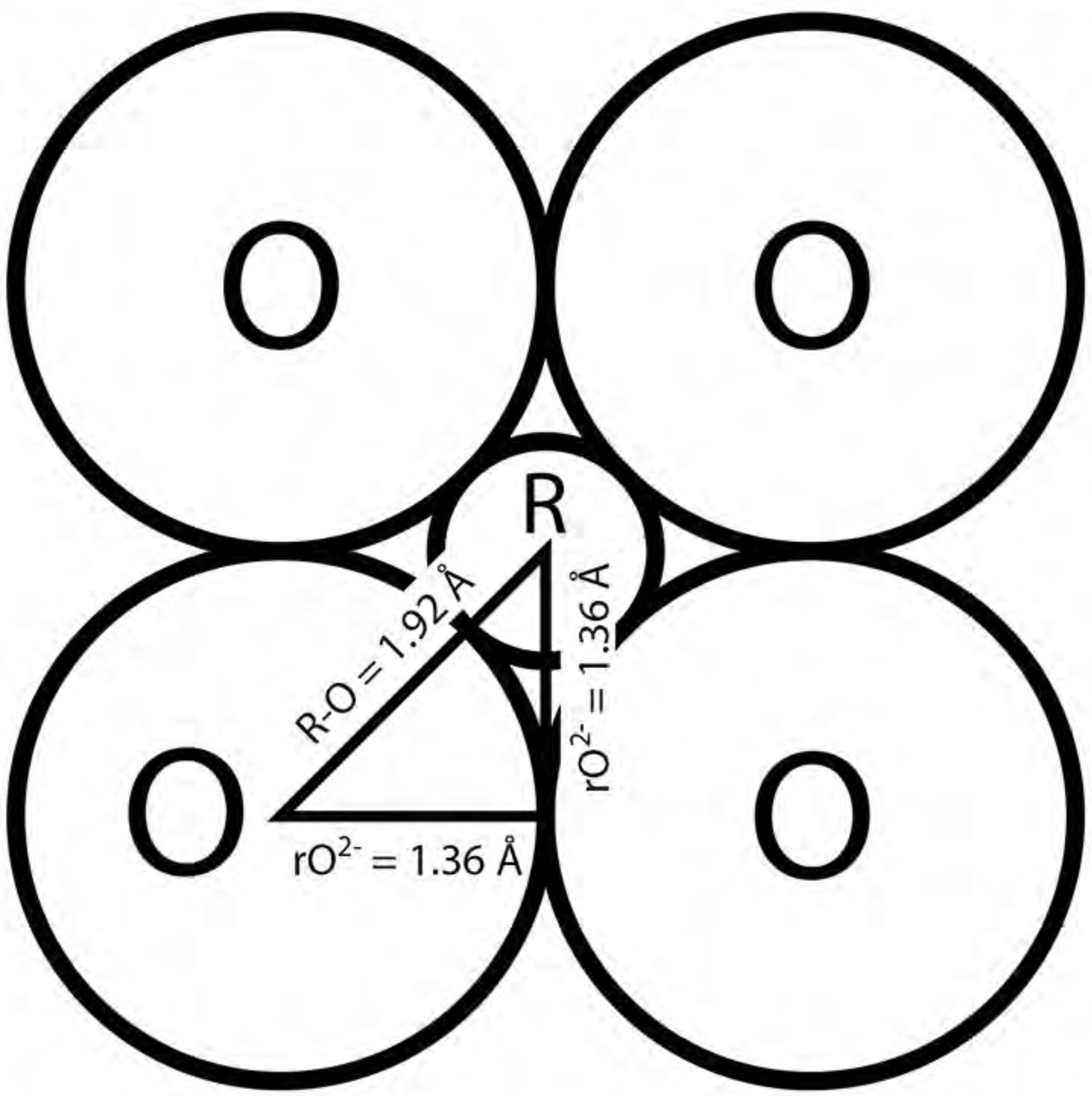


Fig. 11

a



b



c

